ACS APPLIED MATERIALS & INTERFACES

www.acsami.org Research Article

# An Oxidative Stress Nanoamplifier with Efficient Non-Fenton-Type Hydroxyl Radical Generation and Sulfur Dioxide Release for Synergistic Treatment of Tumor

Shasha Zhao,[#] Zhonghuan Qu,[#] Likai Wang,[#] Peng Gu, Juan Mou, Shiping Yang, and Huixia Wu*

Cite This: *ACS Appl. Mater. Interfaces* 2025, 17, 16681−16695 Read Online

ACCESS | Metrics & More | Article Recommendations | Supporting Information

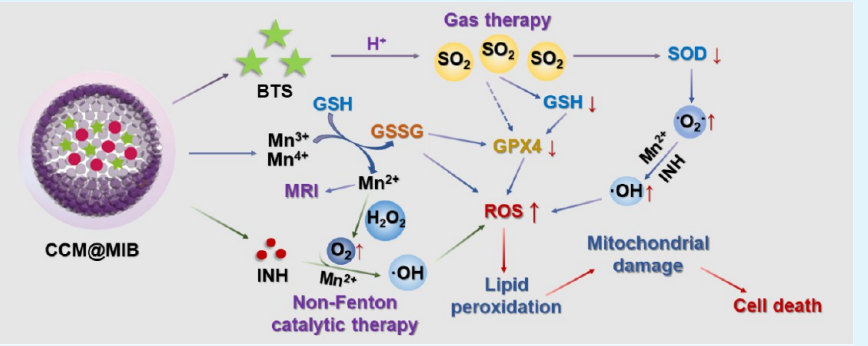


**ABSTRACT:** Overcoming tumor antioxidant defenses remains a critical challenge for reactive-oxygen-species-mediated tumor therapies. To address this problem, herein, a theranostic nanomedicine designated as CCM@MIB has been elaborately constructed. Homologous cancer cell membrane (CCM) camouflage significantly enhances the selective accumulation of the nanomedicine at tumor sites. In response to the tumor microenvironment (TME), CCM@MIB controllably releases Mn ions and sulfur dioxide ($SO_2$) molecules. The released Mn ions catalyze the self-oxidation of isoniazid to generate highly toxic •OH, while the $SO_2$ produced by benzothiazole sulfinate effectively disrupts tumor antioxidant defense systems. The catalase-like activity endowed by Mn ions and the increased intracellular $•O_2^-$ level induced by $SO_2$ further promote •OH production. Therefore, such an intellectual combination of non-Fenton-type catalytic therapy and $SO_2$ gas therapy significantly amplifies oxidative stress and efficiently suppresses tumor growth. Additionally, the TME-activated magnetic resonance imaging contrast performance of CCM@MIB is beneficial for guiding antitumor treatment. This considerate strategy designed in our work provides an ingenious paradigm for the development of efficient antitumor therapies.

**KEYWORDS:** *non-Fenton-type generation of hydroxyl radical, $SO_2$ gas therapy, amplification of oxidative stress, magnetic resonance imaging, homologous tumor targeting*



## 1. INTRODUCTION

Malignant tumors, a leading cause of global health concerns, continue to drive the development of innovative therapeutic strategies. Among emerging approaches, reactive oxygen species (ROS)-mediated noninvasive therapies, particularly chemodynamic therapy (CDT), have aroused extensive attention thanks to their promising antitumor effects and biosafety.[1,2] CDT exploits Fenton or Fenton-like reactions for the purpose of transforming endogenous hydrogen peroxide ($H_2O_2$) in the tumor microenvironment (TME) into highly toxic hydroxyl radicals (•OH), thus causing oxidative damages to tumor cells.[3] CDT breaks through the limitation of ROS production by external stimulations, thereby avoiding insufficient penetration of external stimuli or side effects of external stimuli on normal tissues. However, Fenton reactions still face harsh reaction environment and poor reaction efficiency, which limit the therapeutic effects.[4−6] Therefore, it is urgently needed to develop alternative efficient •OH generation strategies.[7,8]

Intriguingly, isoniazid (INH), a widely utilized antituberculosis drug, does not cause damage to deoxyribonucleic acid (DNA) when used alone. In contrast, in the presence of Mn(II) or Mn(III) ions, INH is able to induce the break of DNA single and double strands in cells as these Mn ions could catalyze the self-oxidation of INH (with the participation of $O_2$

Received: January 18, 2025
Revised: February 24, 2025
Accepted: March 3, 2025
Published: March 8, 2025

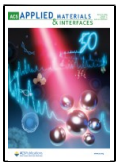




https://doi.org/10.1021/acsami.5c01310
*ACS Appl. Mater. Interfaces* 2025, 17, 16681−16695

**Scheme 1. Schematic Diagram for the Construction of CCM@MIB and the Mechanism of Tumor Catalytic-Gas Combination Therapy**

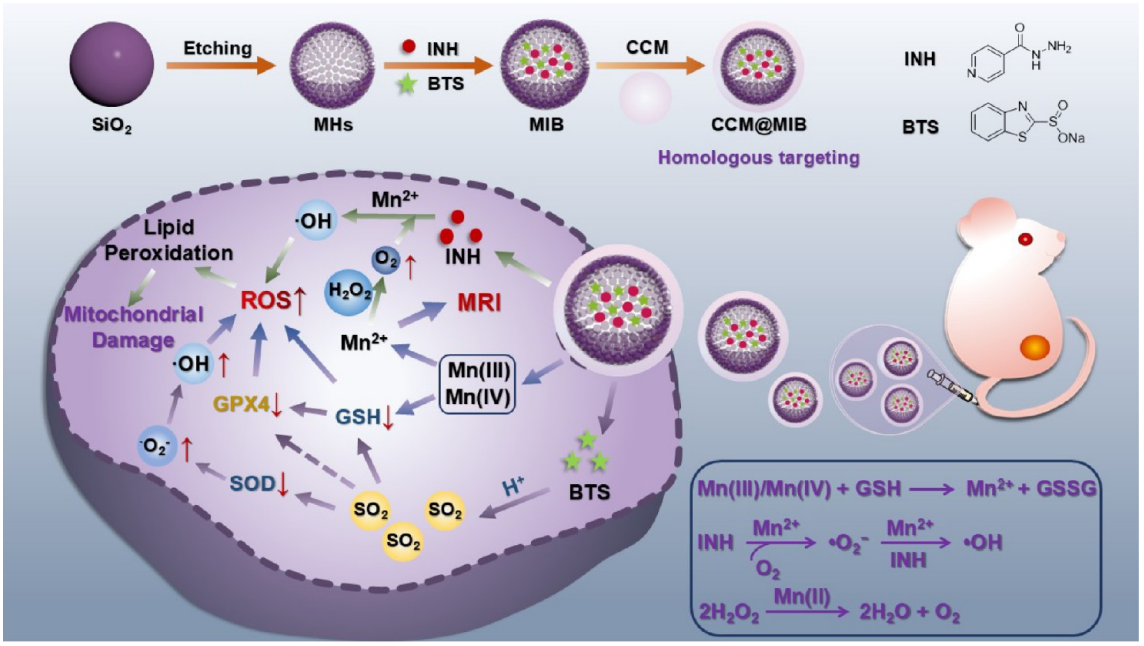


molecules) to generate highly toxic •OH.[9] The damage to DNA is effectively mitigated by superoxide dismutase (SOD) and •OH scavengers rather than catalase (CAT), indicating that •OH is generated from superoxide ($•O_2^-$) radicals, which is the intermediate from the self-oxidation of INH.[9] Such non-Fenton-type •OH generation could be utilized to develop novel •OH-based catalytic therapeutic strategies as an alternative to conventional CDT.[10]

However, in tumor tissues, the powerful antioxidant defense systems would severely reduce the ROS availability.[11] There exist in tumor tissues various antioxidant enzymes, for instance, glutathione S-transferase, glutathione (GSH) peroxidase (GPX), and SOD.[12] Meanwhile, there is a high level of GSH with the range of 2−10 mM in tumor cells, which demonstrates robust ROS scavenging ability.[13] Therefore, it is difficult to achieve ideal antitumor effects only by non-Fenton-type catalytic therapy. If this emerging catalytic treatment is combined with therapeutic agents that can inhibit the tumor antioxidant defense systems, it is expected to significantly amplify oxidative stress and efficiently kill tumor cells.

Sulfur dioxide ($SO_2$), an emerging gas therapy (GT) agent after nitric oxide, carbon monoxide, and hydrogen sulfide,[14−16] can efficiently suppress tumor antioxidant defense systems due to its outstanding characteristics.[17] It can deplete the overexpressed GSH in tumor cells by the reaction between oxidized glutathione (GSSG) and $HSO_3^-$ under the catalysis of thioltransferase[18] and convert GSH into S-sulfoglutathione, disrupting the normal cycle of GSH.[19,20] $SO_2$ can inhibit SOD activity,[21,22] which significantly increases intracellular $•O_2^-$ concentration. It can also suppress GPX4 activity in the GSH redox system as well, probably owing to GSH depletion.[23−25] Additionally, in the cells, $SO_2$ is capable of converting into diverse reactive sulfur species during its self-oxidation process.[26] All these behaviors can cause extensive oxidative stress within tumor cells and lead to cell apoptosis.[27−30] Considering these remarkable properties of $SO_2$, we hypothesize that integrating non-Fenton-type •OH generation with $SO_2$-mediated antioxidant suppression could synergistically enhance oxidative damage, addressing the limitations of stand-alone catalytic therapies.

To validate this hypothesis, a theranostic nanomedicine designated as CCM@MIB was ingeniously constructed by using manganese-doped hollow mesoporous silica nanoparticles (MHs) as the carriers, INH and acid-responsive prodrug benzothiazole sulfinate (BTS) as the cargo drugs, and homologous cancer cell membrane (CCM) as the surface camouflage (Scheme 1). Homologous CCM camouflage could significantly augment the selective accumulation of the nanomedicine at tumor sites, while reducing its retention in normal tissues.[31,32] The obtained nanomedicine could controllably release Mn ions and produce $SO_2$ in response to the TME. Importantly, the released Mn ions would catalyze self-oxidation of the loaded INH to generate highly toxic •OH, while the $SO_2$ produced from BTS could effectively inhibit tumor antioxidant defense systems. Besides, the CAT activity of MHs and the increased intracellular $•O_2^-$ concentration caused by $SO_2$ would enhance the non-Fenton-type catalytic therapy effect. Therefore, the cooperation of such non-Fenton-type catalytic therapy with $SO_2$ GT remarkably amplifies oxidative stress and effectively kills tumor cells, as confirmed by the favorable antitumor outcomes. Additionally, the specific release of Mn ions in response to TME makes CCM@MIB promising as an activated $T_1$-weighted magnetic resonance imaging (MRI) contrast agent for guiding antitumor treatment. This innovative synergistic treatment model developed in this contribution is anticipated to offer an effective strategy for efficient and precise tumor treatment.

## 2. EXPERIMENTAL SECTION

**2.1. Synthesis of $SiO_2$ Nanoparticles.** In brief, ammonia (2.5 mL), ethanol (50 mL), and water (1.5 mL) were mixed together and immersed in a water bath (65 °C). Tetraethyl protosilicate (1.9 mL) was then added to the mixture with a syringe pump (nearly 2.5 h), and the solution was vigorously blended and kept under reaction at 65


https://doi.org/10.1021/acsami.5c01310
ACS Appl. Mater. Interfaces 2025, 17, 16681−16695

°C for 4 h. Then, the mixture after the reaction was exposed to centrifugation at 11 000 rpm, and the collected solid was purified by water and ethanol (three times). The obtained $SiO_2$ nanoparticles were finally kept dispersed in water.

**2.2. Synthesis of MHs.** MHs were prepared through a hydrothermal process. 169 mg of $MnSO_4{\cdot}H_2O$ and 92.5 mg of disodium maleate were dissolved in 18 mL of water. Then, 30 mg of $SiO_2$ nanoparticles were evenly dispersed in the as-prepared solution. This mixture was added into a tetrafluoroethylene vessel (25 mL), which was sealed within a stainless-steel autoclave, and the autoclave was heated in the oven (180 °C, 12 h). After the temperature of the autoclave was cooled to room temperature naturally, the mixture was centrifuged (11 000 rpm) and the resulting solid was cleaned using water (three times) and finally dispersed in water.

**2.3. Loading INH and BTS in MHs (MIB).** A phosphate-buffered saline (PBS) solution (20 mL) containing INH (2 mg $mL^{-1}$) and BTS (1 mg $mL^{-1}$) was prepared. Under magnetic stirring at 600 rpm, 20 mg of MHs were added into the mixture, and the solution was under vigorous agitation (room temperature, in the dark, 12 h). The mixture was then subjected to centrifugation at 16 000 rpm. Next, the collected solid was carefully rinsed utilizing PBS (three times) and finally dispersed with PBS for later use.

In order to work out the drug loading capacity, the absorbance intensities of a series of standard BTS solutions were recorded at 294 and 263 nm, and the data for the standard INH solutions were determined at 263 nm; thus, standard curves of BTS and INH were plotted. The quantities of loaded BTS and INH were determined by, respectively, subtracting the amounts of unloaded INH and BTS, which were derived from the absorbance of the collected supernatant as well as the standard curves of INH and BTS. Drug loading capacities were determined using this formula: Drug loading capacity (%) = (mass of drug loaded)/(total MIB mass) × 100%.

**2.4. Coating the Homotypic CCM on MIB (CCM@MIB).** The cell membranes of 4T1 cells were extracted with a membrane protein extraction kit and dispersed in PBS solution. Next, the membrane solution (2 mg $mL^{-1}$, 0.5 mL) was filtered for more than 10 times through the polycarbonate membrane (400 nm) with the aid of an Avanti Mini-Extruder. Finally, the PBS solution of the cell membranes was uniformly mixed with the PBS solution of MIB (2 mg $mL^{-1}$) with an equal volume and filtered over 10 times through the polycarbonate membrane (200 nm). The treated solution was centrifuged at 4 °C (6000 rpm, 10 min), and the collected CCM@MIB was dispersed in the PBS solution and stored at 4 °C.

**2.5. Release of Mn Ions.** Mn ion release from MIB cultivated under varying conditions was under assessment with inductively coupled plasma-atomic emission spectrometry (ICP-AES). Four experiments were allocated (PBS solutions): (1) pH = 7.4, (2) pH = 6.5, (3) pH = 5.0, and (4) pH = 5.0 + 5 mM GSH. MIB was diluted separately with the above solutions (50 $\mu$g $mL^{-1}$, 8 mL), wrapped in dialysis bags with an MWCO of 3500 Da, and placed into the corresponding PBS solution (20 mL, 37 °C). After that, the dialyzate of 4 mL was removed at different time-points for ICP-AES measurement. Meanwhile, an equivalent volume of fresh PBS solution was supplied into the solution.

**2.6. $O_2$ Generation Measurement.** The dissolved oxygen level was tracked in real-time using a dissolved oxygen meter. Four groups were assigned as (1) pH 7.4 + 10 mM $H_2O_2$, (2) pH 7.4 + 200 $\mu$g $mL^{-1}$ MHs + 10 mM $H_2O_2$, (3) pH 6.5 + 200 $\mu$g $mL^{-1}$ MHs + 10 mM $H_2O_2$, and (4) pH 5.0 + 200 $\mu$g $mL^{-1}$ MHs + 10 mM $H_2O_2$. The concentrations of dissolved oxygen were measured every 5 min, and the total monitoring time was 30 min.

**2.7. GSH Consumption Assay.** 5,5′-Dithiobis(2-nitrobenzoic acid) (DTNB) was employed to investigate the GSH depletion ability of MIB. MIB (50, 100, 200, 300, or 400 $\mu$g $mL^{-1}$) was mixed with the PBS solutions (pH = 7.4, 6.5, or 5.0), which contain GSH (1 mM), and cultured for 2 or 6 h at 37 °C. Next, 50 $\mu$L of the supernatant was diluted to 2 mL with PBS solution (pH = 7.4). The DTNB solution (100 mM, 10 $\mu$L) was then added, and the absorbance intensities of the solution were measured using ultraviolet−visible (UV−vis) spectroscopy. Finally, the removal efficiency of GSH was calculated on the basis of the absorbance value at 412 nm by utilizing the standard GSH curve.

**2.8. Detection of •OH Generation in Solutions by Tetramethylbenzidine (TMB).** The production of •OH from the materials in solutions without $H_2O_2$ was detected using TMB as a probe. MIB was dispersed in the PBS solution (3 mL, pH 5.0, 6.5, or 7.4) with varying concentrations, namely, 25, 50, 100, and 200 $\mu$g $mL^{-1}$, and TMB (0.03 M, 80 $\mu$L) was added into the solutions. The absorbances of the mixtures from 400 to 800 nm after different reaction times were quantified using UV−vis spectroscopy.

**2.9. Detection of $SO_2$ Release in Solutions.** The generation of $SO_2$ was detected with 7-diethylaminocoumarin-3-aldehyde (DEACA) as a fluorescence (FL) probe. The standard $NaHSO_3$ solutions prepared with PBS (2 mL) were uniformly blended with DEACA (100 mM, 100 $\mu$L). After incubation for 10 min, the FL spectra ($\lambda_{ex}$ = 390 nm) of the solutions in the range of 400−600 nm were measured, and then, the standard $NaHSO_3$ curve was graphed based on the FL intensities of the solutions at 483 nm.

BTS or MIB (200 $\mu$g $mL^{-1}$) was cultured in 2 mL of PBS (pH = 5.0, 6.5, or 7.4) for a predetermined period of time. Then, 100 $\mu$L of DEACA with a concentration of 100 $\mu$M was added into the above solutions and incubated for 10 min. Finally, the FL intensities of various samples were detected (experiment parameters: $\lambda_{ex}$ = 390 nm and $\lambda_{em}$ = 483 nm), and the amount of released $SO_2$ was calculated based on the standard curves.

**2.10. MRI of MIB in Solutions.** Four MIB solutions (15 mM) were prepared using the following PBS solutions: (1) pH = 7.4, (2) pH = 6.5, (3) pH = 5.0, and (4) pH = 5.0 + 5 mM GSH. The as-prepared MIB solutions were incubated (37 °C, 110 rpm) for 12 h and then diluted with the corresponding buffer to prepare the working solutions (1.5 mL) with various Mn concentrations (0, 0.3, 0.6, 0.9, 1.2, and 1.5 mM). The MRI images and relaxation rates of the MIB solutions were recorded on an NMI20-Analyst MRI analyzer (0.5 T). The Mn contents within the materials were quantified by using ICP-AES. $T_1$- and $T_2$-weighted MRI scannings were performed with routine spin−echo sequences ($T_1$: waiting time (TW) = 18 000 ms, echo time (TE) = 0.04 ms, repetition time (TR) = 500 ms; $T_2$: TW = 8000 ms, TE = 400 ms, TR = 5000 ms).

**2.11. Cell Culture.** Human umbilical vein endothelial cells (HUVECs) as well as 4T1 murine breast tumor cells were acquired from the Fudan University Shanghai Cancer Center. HUVECs were cultured in Dulbecco's modified Eagle medium (DMEM) supplemented with both 10% fetal bovine serum (FBS) and 1% antibiotic mixture (penicillin−streptomycin) at 37 °C in a humidified atmosphere which contains 5% $CO_2$. Similarly, Roswell Park Memorial Institute (RPMI) 1640 was used for 4T1 cells under culture conditions identical to those used for HUVECs.

**2.12. Assay of Cellular Uptake.** 4T1 cells ($1 \times 10^6$ cells per well) cultured in 6-well plates were incubated with CCM@MIB (a concentration of 200 $\mu$g $mL^{-1}$, 1 mL) for 0−6 h. The tumor cells were gathered after the removal of the redundant material, and ICP-AES was employed to analyze the intracellular Mn content and evaluate the uptake of CCM@MIB by cells.

**2.13. Homologous Targeting.** To facilitate the observation of material uptake, rose Bengal (RB) was loaded into MHs, and finally, the hollow spheres were coated with a 4T1 cell membrane. Then, 4T1 cells, CT26 cells, and HUVECs cultured separately in confocal culture dishes ($2 \times 10^5$ cells per well) were coincubated with the CCM@MH@RB (200 $\mu$g $mL^{-1}$, 1 mL) for 4 h. After eliminating the redundant material, the uptake of CCM@MH@RB by different groups of cells ($\lambda_{ex}$ = 548 nm, $\lambda_{em}$ = 540−590 nm) was monitored using confocal laser scanning microscopy (CLSM).

**2.14. *In Vitro* Cytotoxicity.** *In vitro* cytotoxicities of CCM@MH against 4T1 cells and CCM@MIB against HUVECs were assessed with the methylthiazolyldiphenyl-tetrazolium bromide (MTT) assay. Initially, the cells ($1 \times 10^4$ cells per well) were seeded in 96-well plates and then cultured with various concentrations of materials (0, 10, 20, 50, 100, and 200 $\mu$g $mL^{-1}$) for different time periods (12 and 24 h). The cell viabilities were then measured by the MTT assay.


https://doi.org/10.1021/acsami.5c01310
ACS Appl. Mater. Interfaces 2025, 17, 16681−16695

**2.15. *In Vitro* •OH and $SO_2$ Combined Therapy.** *In vitro* therapeutic efficacies of CCM@MIB were evaluated by the MTT assay as well as calcein acetoxymethyl ester (calcein-AM)/propidium iodide (PI) staining. For the MTT assay, the experiments were assigned into four groups: (1) CCM@MH, (2) CCM@MI, (3) CCM@MB, and (4) CCM@MIB. 4T1 cells ($1 \times 10^4$ cells per well) attached in 96-well plates were coincubated with the materials (0, 10, 20, 50, 100, and 200 $\mu$g mL$^{-1}$) for 12 h. Then, MTT was utilized to assess the cell viability.

To make living and dead cells visible, 4T1 cells ($2 \times 10^5$ cells per well) were cultured for 4 h with the materials at a concentration of 200 $\mu$g mL$^{-1}$. Then, they were cleaned three times with PBS, followed by calcein-AM and PI staining. After the removal of excess dyes, the tumor cells were exposed to CLSM observation (parameters for calcein-AM: $\lambda_{ex}$ = 490 nm and $\lambda_{em}$ = 500−550 nm; parameters for PI: $\lambda_{ex}$ = 535 nm and $\lambda_{em}$ = 580−640 nm).

**2.16. *In Vitro* Release of $SO_2$ and Intracellular ROS Generation.** Five groups were allocated in the evaluation experiments: (1) PBS for control, (2) CCM@MH, (3) CCM@MI, (4) CCM@MB, and (5) CCM@MIB. $SO_2$ release in tumor cells was tested with DEACA. Tumor cells were incubated with 1 mL of the materials from various groups (200 $\mu$g mL$^{-1}$) for a duration of 4 h in laser confocal Petri dishes of 35 mm ($2 \times 10^5$ cells per well). Then, 1 mL of the solution of DEACA (5 $\mu$M) was introduced into the dishes, and the cells were cultured with the DEACA (30 min). At last, the $SO_2$ amount within tumor cells was observed with CLSM ($\lambda_{ex}$ = 405 nm, $\lambda_{em}$ = 450−500 nm).

Dihydroethidium (DHE) was utilized to monitor intracellular $\bullet O_2^-$ levels. 4T1 cells and 1 mL of DHE solution (10 $\mu$M) were coincubated for 0.5 h after different treatments. Eventually, intracellular $\bullet O_2^-$ levels were imaged by CLSM (parameters: $\lambda_{ex}$ = 488 nm and $\lambda_{em}$ = 580−630 nm). Intracellular ROS production was evaluated by using 2′,7′-dichlorofluorescin diacetate (DCFH-DA). 4T1 cells ($2 \times 10^5$ cells per well) were cultured in Petri dishes (35 mm) along with the materials for 4 h. After the excess materials were removed, the cells were dyed with DCFH-DA (10 $\mu$M, 1 mL) for 20 min. The ROS content within tumor cells was evaluated by CLSM ($\lambda_{ex}$ = 488 nm and $\lambda_{em}$ = 500−550 nm).

**2.17. Detection of the SOD Activity, Malondialdehyde (MDA) Amount, GSH Level, and GPX4 Activity.** The detection experiments have been divided into five groups for each item: (1) PBS set as control, (2) CCM@MH, (3) CCM@MI, (4) CCM@MB, and (5) CCM@MIB. The volume and concentration of the material solutions were set as 1 mL and 200 $\mu$g mL$^{-1}$, respectively. 4T1 cells ($1 \times 10^6$ cells per well, 6-well plates) were cultured with various groups of materials for 4 h. After that, the cells were gathered in preparation for the next assessment. SOD activities were measured with a total SOD assay kit through the measurement of absorbance intensity at 560 nm. The MDA amounts were assessed with a lipid oxidation (LPO) detection kit by recording an absorbance value of 532 nm. The GSH amounts were detected using a GSH and GSSG assay kit through absorbance measurements at 412 nm. The GPX4 activities were acquired with a GPX assay kit by means of detecting the absorbance at 340 nm.

**2.18. Measurement of Mitochondrial Membrane Potential.** The variation in mitochondrial membrane potential within the cells was assessed using a 5,5′,6,6′-tetrachloro-1,1′,3,3′-tetraethylbenzimidazolocarbocyanine (JC-1) assay kit, and the experimental grouping was the same as that of cellular ROS measurement. In brief, 4T1 cells ($2 \times 10^5$ cells per well, CLSM-exclusive dishes) were allowed to culture in the presence of materials (200 $\mu$g mL$^{-1}$, 1 mL) for 4 h. After gentle rinsing with PBS, 1 mL of solution for JC-1 staining was added, and the influences of various treatments on the potential of the mitochondrial membrane were measured with CLSM. The parameters are as follows: JC-1 monomer: $\lambda_{ex}$ = 488 nm and $\lambda_{em}$ = 500−560 nm; JC-1 polymer: $\lambda_{ex}$ = 543 nm and $\lambda_{em}$ = 560−610 nm.

**2.19. Hemolysis.** The hemolysis evaluations were assigned to seven groups: PBS (the negative control group), $H_2O$ (the positive control group), and five experimental groups of CCM@MIB (50, 100, 200, 400, and 600 $\mu$g mL$^{-1}$). Each group was measured in parallel three times. Fresh blood was obtained from 6-week-old mice by an ocular enucleation procedure, and then, the erythrocytes were isolated through centrifugation (1500 rpm). After being rinsed sufficiently with PBS to remove serum and other impurities, the erythrocytes were uniformly dispersed in PBS (9 mL). The PBS solutions (with a volume of 1 mL) of CCM@MIB with different concentrations were blended with the erythrocyte suspension (400 $\mu$L), and the mixtures were kept standing for 4 h. The absorbance intensity of the supernatants after centrifugation (1500 rpm) was recorded at 541 nm for calculating the hemolysis rate.

$$\text{Hemolysis rate}(\%) = 100\% \times \frac{\text{Abs(experiment group)} - \text{Abs(negative control)}}{\text{Abs(positive control)} - \text{Abs(negative control)}}$$

**2.20. Tumor Model Establishment.** BALB/c mice (female, 5 weeks old) were purchased from Jiangsu Aniphe Biolaboratory Inc. (China). All experimental procedures and animal care were carried out consistent with the national and local Guidelines for the Care and Use of Laboratory Animals (China). In addition, the animal experiments were approved by the Experimental Animal Management and Animal Welfare Ethics Committee of Shanghai Normal University. To establish a tumor model, the mice were injected subcutaneously with 4T1 cells (density of $2.0 \times 10^6$ cell/mL, 100 $\mu$L) in the right hind limbs. *In vivo* MRI and therapies could be performed after the volume of the tumor increased to 100 mm$^3$.

**2.21. *In Vivo* MRI.** A 1 T MRI scanner (NM42−040H−I) was employed to perform the *in vivo* $T_1$-weighted MRI. Mice bearing tumors were anesthetized through the intraperitoneal injection of 10 wt % chloral hydrate solution, followed by intravenous injection with the PBS solution of CCM@MIB (25 mg kg$^{-1}$, 120 $\mu$L). MRI images of the mice were acquired after injection (2, 4, 6, 8, and 10 h). The mice prior to injection (0 h) were regarded as the blank control group. MRI parameters: TE = 20 ms, TR = 500 ms, slice thickness = 1.7 mm, slice gap = 2.0 mm, field of view = 100 × 100 mm, and matrix = 256 × 192 mm.

**2.22. *In Vivo* Combined Therapeutic Effect.** Mice bearing 4T1 tumors were divided into five groups (eight mice per group) at random: (1) Control (PBS), (2) CCM@MH, (3) CCM@MI, (4) CCM@MB, and (5) CCM@MIB. On days 0 and 8, the mice were administrated with the materials (25 mg kg$^{-1}$, 120 $\mu$L) through tail-vein injection. At 6 h after the second injection, one mouse in every group was chosen at random, and the tumors were dissected and stained with DCFH-DA to measure ROS levels within tumor tissues. GPX4 immunofluorescence staining was conducted on the sections of tumor taken from another mouse in each group. DEACA staining was carried out on tumors, kidneys, and livers of every group to detect *in vivo* $SO_2$ release. Another mouse was also selected randomly from each group, and then, the tumors were resected for terminal deoxynucleotidyl transferase dUTP nick-end labeling (TUNEL) and hematoxylin and eosin (H&E) stainings. Both tumor volumes and body weights of the mice were measured (every other day) during 16 days of treatment. The calculation of tumor volume: volume = 0.5 × (length × width$^2$). After monitoring for 16 days, the major organs within groups 1 and 5 were collected for the purpose of histological analysis. Additionally, blood was harvested from the eyes in these two groups for biochemical analysis (kidney and liver indexes) as well as a blood routine test.

**2.23. Statistical Analysis.** Statistical analysis utilized a two-tailed unpaired Student's *t* test. Data were represented as mean ± standard deviation. Specifically, $^*p < 0.05$ was regarded as statistically significant, while $^{**}p < 0.01$, $^{***}p < 0.001$, and $^{****}p < 0.0001$ were treated as extremely significant.

## 3. RESULTS AND DISCUSSION

**3.1. Synthesis and Characterization.** MHs were obtained through a one-pot hydrothermal reaction in which $SiO_2$ nanoparticles served as the template, disodium maleate acted as the etchant, and $MnSO_4 \bullet H_2O$ was employed as the dopant. The initial $SiO_2$ nanoparticles exhibit a uniform spherical morphology with a mean particle size of ∼90 nm (Figure S1). Under high-temperature hydrothermal conditions,


https://doi.org/10.1021/acsami.5c01310
ACS Appl. Mater. Interfaces 2025, 17, 16681−16695

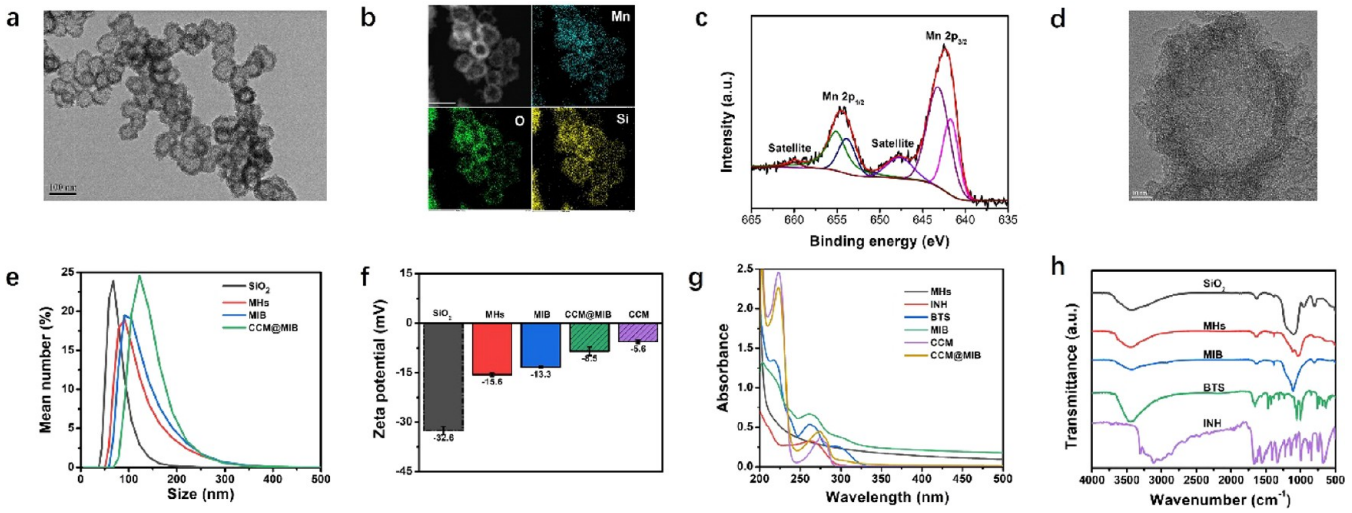


**Figure 1.** Compositional and structural characterizations. (a) TEM image of MHs. (b) Energy-dispersive X-ray spectroscopy elemental mapping images of MHs. Scale bar: 100 nm. (c) High-resolution XPS spectra of Mn 2p for MHs. (d) TEM image of CCM@MIB. (e) Hydrodynamic size distribution of $SiO_2$, MHs, MIB, and CCM@MIB dispersions. (f) Zeta potentials of $SiO_2$, MHs, MIB, CCM@MIB, and CCM in water. (g) UV−vis absorption spectra of MHs, INH, BTS, MIB, CCM, and CCM@MIB. (h) FTIR spectra of $SiO_2$, MHs, MIB, BTS, and INH.

the interior of $SiO_2$ templates gradually dissolved, and meanwhile, the released $SiO_2$ oligomers interacted with the Mn precursors, forming Mn-doped silica layers deposited on the $SiO_2$ shells. With the continuous dissolution and deposition process, the MHs were finally formed.[33] Both scanning electron microscopy (SEM) and transmission electron microscopy (TEM) images (Figures 1a and S2) demonstrate that MHs own a well-defined cavity structure, and their shells are composed of many small vesicles. According to the statistics on 100 nanoparticles at random from the TEM images, the diameter and shell thickness of the obtained MHs were calculated to be about 93 and 13 nm (Figure S3), respectively. The doping of Mn ions is verified by energy-dispersive spectroscopy (Figure S4). The elemental mapping images reveal that O, Mn, and Si are evenly distributed in the shell of the hollow nanospheres (Figure 1b). The doping amount of Mn ions in MHs was measured to be 1.14 mmol $g^{-1}$ by ICP-AES. Nitrogen ($N_2$) adsorption/desorption measurement results indicate that MHs possess a well-defined mesoporous structure. The pore volume, most probable aperture, and surface area (Brunauer−Emmett−Teller) of MHs were calculated to be 0.89 $cm^3$ $g^{-1}$, 6.57 nm, and 542.31 $m^2$ $g^{-1}$, respectively (Figure S5). The mesoporous and hollow structure makes MHs an ideal carrier to encapsulate a variety of drugs for different therapeutic purposes.

X-ray diffraction (XRD) and X-ray photoelectron spectroscopy (XPS) characterizations were performed to confirm the form of Mn ions within the MHs. Powder XRD pattern (Figure S6) reveals that the as-synthesized MHs contain a cubic structure of manganous silicate (JCPDS no. 37−0221), affirming the covalent bonding of the doped Mn in the silica framework. The large and wide peak appearing at around 20° can be attributed to the amorphous silica. The XPS survey spectrum (Figure S7) also identifies that Mn, O, and Si elements exist in MHs. The peak fitting of the Mn 2p spectrum (Figure 1c) shows the existence of Mn $2p_{3/2}$ peaks at 641.7 and 643.2 eV as well as Mn $2p_{1/2}$ peaks at 653.9 and 655.1 eV, which are contributed to both $Mn^{3+}$ and $Mn^{4+}$ species, and their respective amounts were 34% and 66%, indicating that the doped Mn ions exist mainly in the oxidation states of +3 and +4 within MHs.[33−35] The ratio of $Mn^{3+}$ to $Mn^{4+}$ was determined to be about 1:2 by the investigation of the XPS peak areas.

MHs were further loaded with drugs BTS and INH, and then, the resulting MIB was coated with homotypic CCM to obtain the final CCM@MIB nanomedicine. BTS, the $SO_2$ donor, was synthesized following the reported method.[36] Both $^1H$ nuclear magnetic resonance (NMR) and $^{13}C$ NMR spectra (Figure S8a,b) validate the successful synthesis of BTS. The loading capacities of INH and BTS in MIB were calculated to be about 28% and 21%, respectively, by quantitatively analyzing the absorbances at 263 nm (INH) and 294/263 nm (BTS) of the unloaded drugs (Figure S9). After CCM coating, the obtained CCM@MIB was first characterized by TEM (Figure 1d), which showed the coverage of a layer of CCM on the surface of the hollow sphere. The Z-average hydrodynamic size of CCM@MIB (about 131 nm) is significantly larger than that of MIB (97 nm), which is due to the cell membrane coating on the MIB (Figure 1e). The hydrated particle size of MIB (97 nm) is only slightly increased compared to that of MHs (90 nm), because BTS and INH are mainly loaded in the channels and cavities of MHs. The Zeta potential data of the products at each step are presented in Figure 1f. The reasonable alteration of Zeta potentials supports the conclusion that CCM@MIB has been successfully constructed. The UV−vis absorption spectrum of CCM@MIB (Figure 1g) displays only two absorption peaks at 223 and 274 nm, which mainly arise from CCM, while the absorption bands arising from BTS and INH might be covered. To verify that the drugs were loaded in MHs, the Fourier transform infrared (FTIR) spectrum of the MIB was determined. As illustrated in Figure 1h, the characteristic band at 1637 $cm^{-1}$ is ascribed to the stretching vibrations of C═O,[37] clearly indicating the existence of INH. Meanwhile, new absorption peaks located at 1109 and 1207 $cm^{-1}$ refer to the respective stretching vibrations S−O and S═O, verifying that BTS was successfully loaded.[36] Hydrodynamic sizes and Zeta potentials of CCM@MIB in PBS, FBS, and RPMI 1640 were monitored for 7 days, and no significant changes were detected (Figure S10a,b). The photograph of various


https://doi.org/10.1021/acsami.5c01310
ACS Appl. Mater. Interfaces 2025, 17, 16681−16695

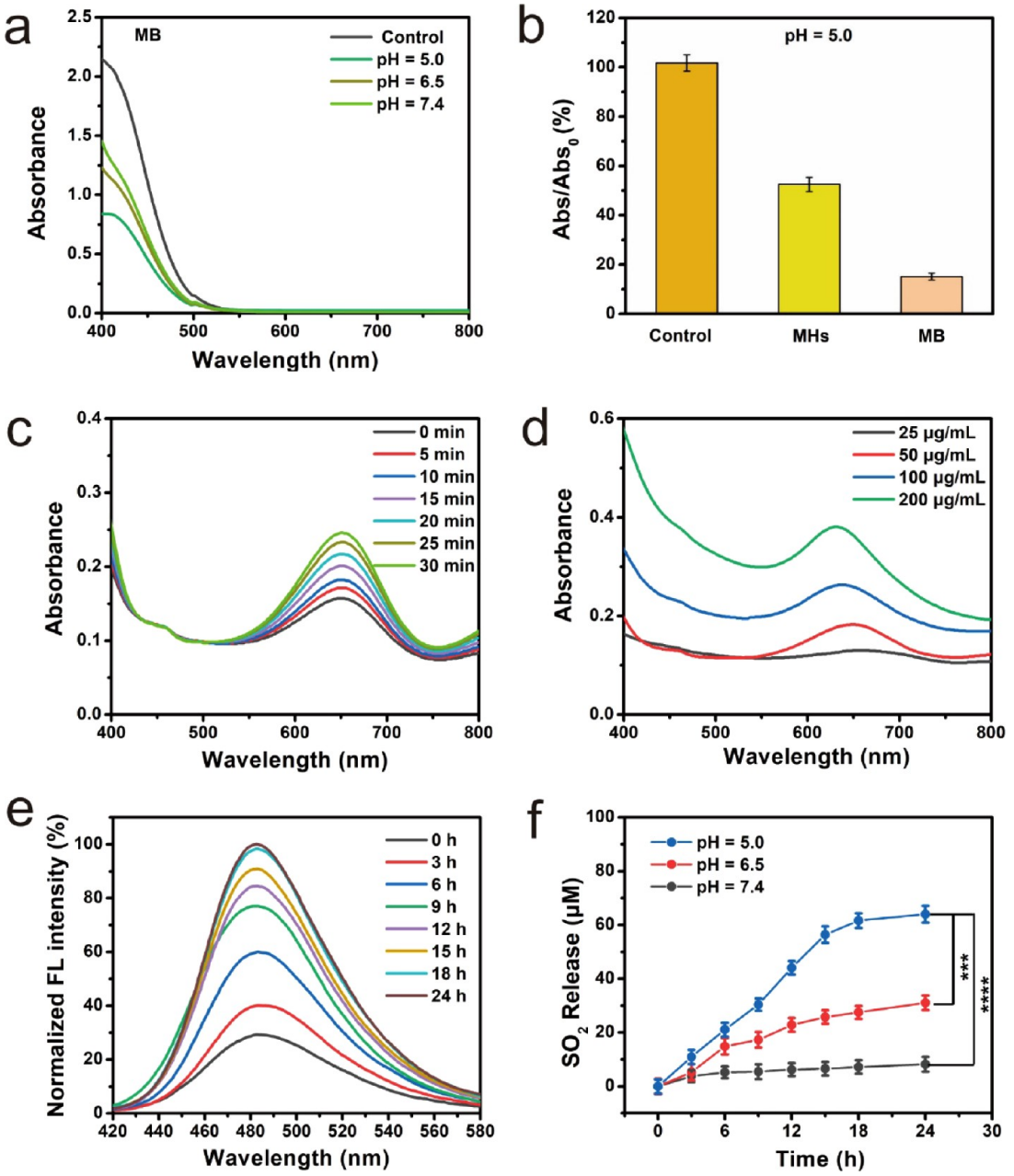


**Figure 2.** *In vitro* evaluation of GSH depletion, •OH generation, and $SO_2$ release ability. (a) GSH (5 mM) depletion ability of MB (282 $\mu$g mL$^{-1}$) containing the same concentration of MHs (200 $\mu$g mL$^{-1}$) at various pH values after 6 h of incubation. (b) Relative GSH (5 mM) depletion capacity of MHs (200 $\mu$g mL$^{-1}$) and MB (282 $\mu$g mL$^{-1}$) containing the same concentration of MHs at pH 5.0. (c) Changes in the absorption spectra of TMB incubated with MIB (200 $\mu$g mL$^{-1}$) for different time periods at pH 5.0. (d) Absorption spectra to assess the oxidation of TMB (30 min) in different concentrations of MIB at pH 5.0. (e) Normalized FL spectra of DEACA incubated with MIB for different time periods at pH 5.0. (f) $SO_2$ release curves of MIB at different pH values.

dispersions (after 7 days of standing) (Figure S10c) also demonstrates the excellent dispersibility of CCM@MIB in physiological solutions.

**3.2. Evaluation of Mn Ion Release and GSH Depletion in Solutions.** The Mn−O bonds within MHs make the hollow spheres easy to degrade in the TME, which facilitates the release of Mn ions.[33] As illustrated in Figure S11, more Mn ions were released from MIB with increasing solution acidity, and the reduction of high-valence Mn by GSH can significantly promote the degradation. The maximum release of Mn ions reached nearly 86% (pH 5.0 and 5 mM GSH). Therefore, reducing and acidic TME can induce the degradation of MIB and facilitate the efficient liberation of Mn ions, conducive to the generation of •OH by non-Fenton-type catalytic reaction and the enhancement of MRI contrast effects at tumor sites.

High levels of GSH in tumor cells are unfavorable for ROS-mediated tumor therapy, because GSH can lead to the off-target consumption of generated ROS and reduce therapeutic efficacy.[38,39] Therefore, GSH depletion may be a smart and efficient way to amplify oxidative stress. Considering the presence of $Mn^{3+}/Mn^{4+}$ within MHs and the fact that GSH can promote Mn ions release, it is believed that MHs own the ability to eliminate GSH.[24] Herein, DTNB, a GSH indicator,[39] was utilized to evaluate the GSH depletion ability of MHs and


https://doi.org/10.1021/acsami.5c01310
ACS Appl. Mater. Interfaces 2025, 17, 16681−16695

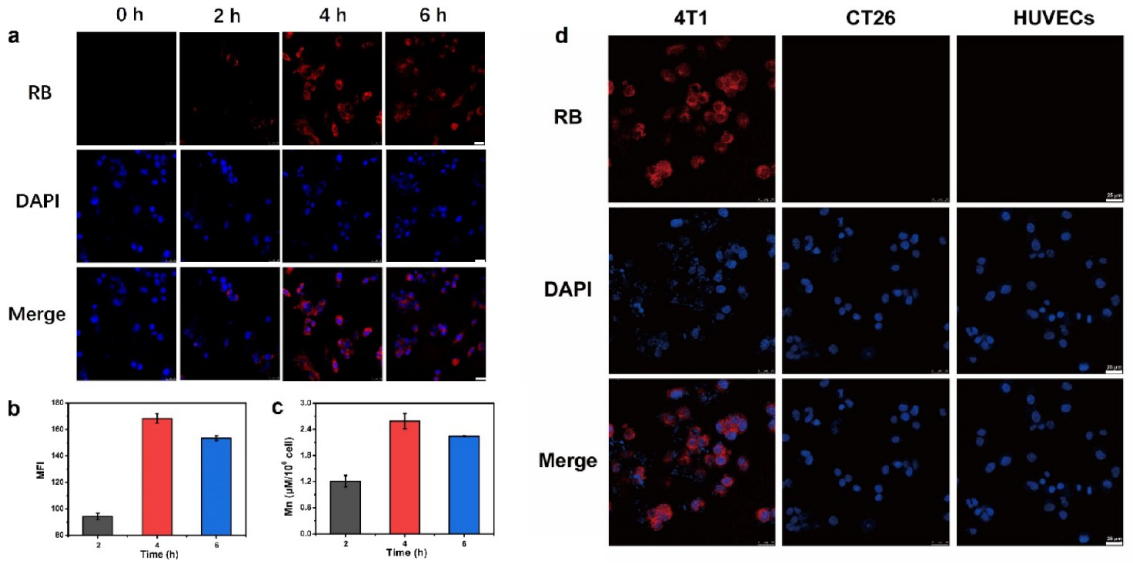


**Figure 3.** *In vitro* cell uptake and homologous targeting evaluation. (a) Confocal microscopy images of 4T1 cells coincubated with CCM@MH@RB (200 $\mu$g mL$^{-1}$) at different incubation time-points. Scale bar: 25 $\mu$m. (b) Mean FL intensity (MFI) of CCM@MH@RB incubated with 4T1 cells after different time periods. (c) The uptake analysis of CCM@MH@RB by 4T1 cells using ICP-AES. (d) Confocal microscopy images of 4T1 cells, CT26 cells, and HUVECs after incubation with CCM@MH@RB (200 $\mu$g mL$^{-1}$) for 4 h. Scale bar: 25 $\mu$m.

MB (Figures 2a,b and S12). The removal ability of MHs and MB to GSH is related to the pH values of the solutions, and the acidic environment is beneficial to GSH depletion. Furthermore, the removal rates of GSH by MB (containing the same concentration of MHs) at different pH values (up to 85% at pH 5.0) are all higher than those by MHs at the corresponding pH condition (Figure 2b), indicating that the $SO_2$ released from BTS also owns the ability to eliminate GSH.[21] The GSH depletion enabled by both MHs and $SO_2$ can avoid the generated •OH from being off-target eliminated, which is conducive to maintaining a high ROS concentration for killing tumor cells.

**3.3. ROS Production and $SO_2$ Generation Measurement in Solutions.** To verify the self-oxidation of INH catalyzed by the released Mn ions, TMB was employed to monitor the generation of •OH at diverse pH values or MIB concentrations. The produced •OH radicals could oxidize TMB, thereby forming blue oxidized-TMB (oxTMB) that exhibits a typical absorption peak located at 652 nm (Figure S13a).[40] Impressively, the absorbance intensity of the MIB + TMB group (652 nm) was obviously raised in a slightly acidic environment (Figures 2c and S13b) in comparison with that under normal physiological pH conditions (Figure S13c). In addition, the amount of generated •OH radicals increased with the elevated MIB concentration (Figure 2d). The absence of oxTMB signals after using isopropyl alcohol as a •OH-specific quenching agent further proved that the self-oxidation of INH catalyzed by Mn ions did produce •OH radicals (Figures 2c and S14a,b). The elevated ROS generation capacity of MIB under mildly acidic conditions makes it a promising non-Fenton therapeutic agent by the utilization of acidic TME. In addition, MHs are anticipated to exhibit CAT-like activity because of the existence of Mn ions, which will further contribute to the generation of non-Fenton-type •OH, since the self-oxidation of INH catalyzed by Mn ions requires the participation of $O_2$ molecules. The CAT-mimicking activity of MHs was evaluated by recording the levels of dissolved $O_2$ using a dissolved $O_2$ meter. For the $H_2O_2$ alone group (pH 7.4), no generation of the $O_2$ could be observed, indicating that the self-decomposition of $H_2O_2$ can be ruled out (Figure S15). However, the $O_2$ production from $H_2O_2$ was significantly enhanced in the presence of MHs at the same pH value. At pH 6.5, MHs still exhibited a good CAT-like ability, indicating that they show potential in relieving tumor hypoxia, and the generated $O_2$ can be further beneficial to efficient non-Fenton-type •OH generation.

Considering that the C−S bonds within BTS could be destroyed in the acidic environment and result in the release of $SO_2$,[41,42] DEACA, which can react with $HSO_3^-$ (in a nucleophilic addition reaction) to form a product with strong blue FL (Figure S16a), was employed to detect $SO_2$ liberation from the donor under diverse pH conditions[30] (Figures S16 and 2e,f). At normal physiological pH (pH = 7.4), MIB caused only weak changes in the FL intensity of DEACA even after incubation for 24 h, indicating negligible $SO_2$ release (Figure S16f). In comparison, under mildly acidic conditions (pH = 6.5 or 5.0), the $SO_2$ release rates were significantly enhanced, as indicated by the time-dependent increase in FL intensity (Figures 2e and S16g). Especially at pH 5.0, the released $SO_2$ reached up to 63.98 $\mu$M within 24 h of incubation (Figure 2f). The $SO_2$ release studies under different pH conditions manifest that MIB can sustainably release $SO_2$ when responding to a weakly acidic environment. This is an important advantage for GT because it can treat tumors without significant side effects on normal tissues and organs.

**3.4. *In Vitro* Cellular Uptake and Homologous Targeting Ability.** Prior to *in vitro* antitumor treatment, the ideal time-point for cellular uptake of CCM@MIB labeled with RB was investigated. Figure 3a,b illustrates the brightest red FL in the cytoplasm when CCM@MH@RB was cultured with 4T1 cells for 4 h. Moreover, ICP-AES analysis also showed that intracellular Mn content increased to the maximum after coincubation of the cells with CCM@MIB for 4 h (Figure 3c). Consequently, 4 h was confirmed as the ideal culture time of CCM@MH for most of the subsequent cell experiments.


https://doi.org/10.1021/acsami.5c01310
ACS Appl. Mater. Interfaces 2025, 17, 16681−16695

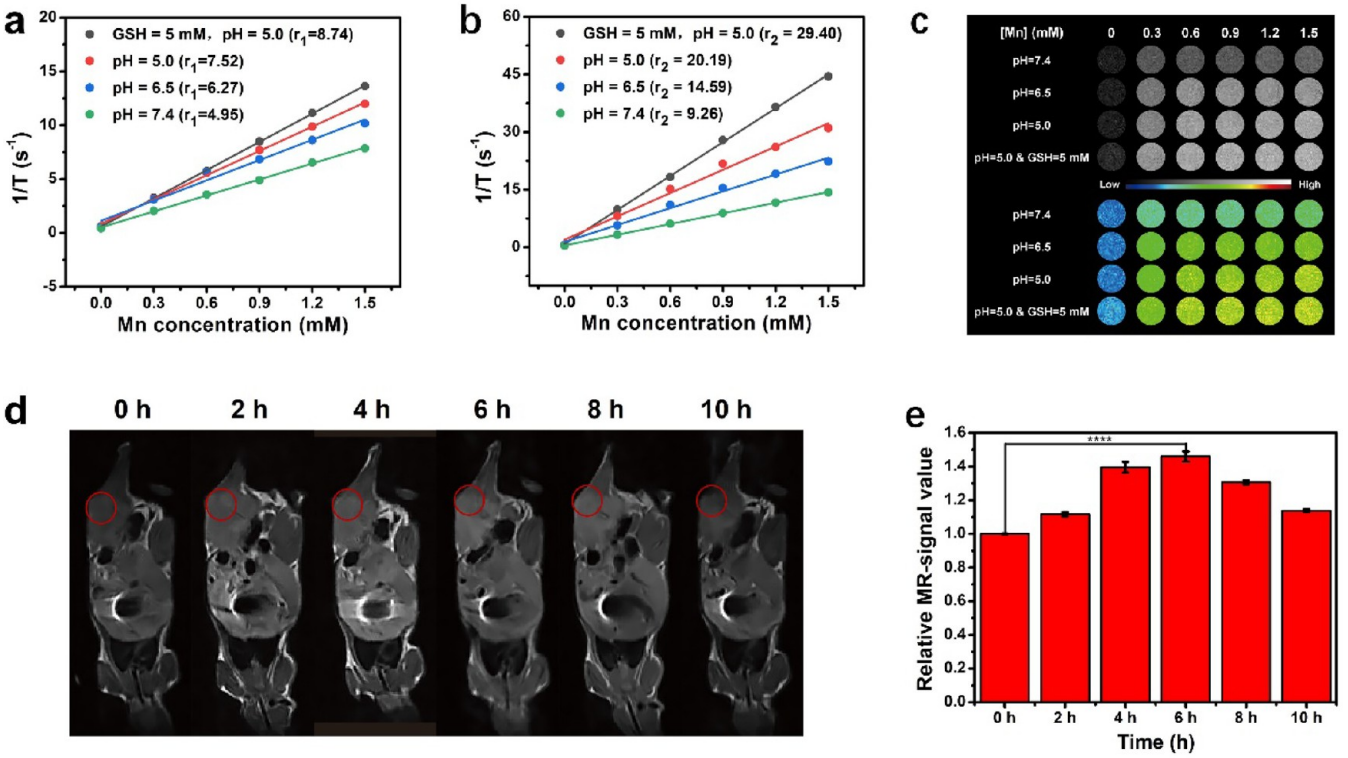


**Figure 4.** MRI performance. Linear regression of (a) $1/T_1$ and (b) $1/T_2$ with Mn concentration in MIB under different conditions. (c) $T_1$-weighted MRI images for MIB with various Mn concentrations at varying pH values with/without GSH. (d) $T_1$ images of mice (tumor-bearing) before (0 h) and after (2, 4, 6, 8, and 10 h) injection of CCM@MIB. (e) Change in relative $T_1$ signal of tumor before and after injecting CCM@MIB.

To explore the targeting ability of CCM@MIB to homotypic tumor cells, the surrogate CCM@MH@RB was incubated with 4T1 cells, CT26 cells, and HUVECs, and the internalization of CCM@MH@RB by the cells was evaluated. Bright FL was observed in 4T1 cells after incubation, while no apparent FL could be found in HUVECs and CT26 cells (Figure 3d), indicating excellent *in vitro* homologous targeting ability of CCM@MH due to highly specific self-targeting adhesive interactions between CCM and 4T1 cells.

**3.5. *In Vitro* and *In Vivo* MRI Studies.** The doping of Mn in MHs and the enhanced release of Mn ions in response to a reducing and acidic environment prompted us to investigate the MRI contrast performances of MIB. The aqueous solutions of MIB showed enhancement of $T_1$ and $T_2$ signals with increasing Mn concentration (Figure S17a). Then, both longitudinal relaxivity $r_1$ and horizontal relaxivity $r_2$ were measured to be only 2.56 and 0.91 $mM^{-1}\cdot s^{-1}$, respectively. Preliminary results indicate that MIB can be utilized as a $T_1$ contrast agent (Figure S17b). With the decrease of solution pH value, the fitted $r_1$ and $r_2$ increased, and the $T_1$ signals were enhanced (Figure 4a,c), indicating that the acidic environment could enhance the $T_1$-weighted MRI contrast ability of MIB. Moreover, the $T_1$ contrast performance of MIB was significantly enhanced by GSH, as indicated by the GSH concentration-dependent increase of $T_1$ signals (Figure S18a–c). Among the experiments shown in Figure 4a,c, the group (pH 5.0 and 5 mM GSH) exhibited the largest relaxation coefficients ($r_1$ = 8.74 and $r_2$ = 29.40) and the strongest $T_1$ contrast effect. The above results confirmed that both acidic and reductive environments could improve the $T_1$-weighted MRI performance of MIB, due to the enhanced liberation of Mn ions under these conditions.

The favorable *in vitro* acid/GSH-responsive $T_1$-weighted contrast enhancement of MIB urged us to further explore the role of CCM@MIB as an activating MRI contrast agent in mice bearing 4T1 tumors. The $T_1$ signal intensity of the tumors was augmented with prolonged time, and it reached the maximum value at 6 h after intravenous injection with CCM@MIB (Figure 4d,e), indicating actively targeted enrichment of the material in tumors and TME-responsive release of $Mn^{2+}$ ions. The satisfactory *in vivo* MRI performance of CCM@MIB suggests that it could be employed as a highly efficient $T_1$ contrast agent to guide antitumor treatment. Additionally, the mean Mn content in the tumor after intravenous injection of CCM@MIB (after 6 h) reached 50 $\mu g\ g^{-1}$ (Figure S19), which was much higher than that of the MIB group (Figure S20), confirming that the CCM camouflage can significantly reinforce the accumulation of the nanomedicine toward tumor sites due to its strong homologous targeting capacity.

**3.6. *In Vitro* Toxicity, Hemolysis, and Antitumor Therapy.** Using HUVECs as a cell model, the cytotoxicity of CCM@MIB on normal cells was evaluated by MTT. The results (Figure S21) revealed that CCM@MIB showed no significant toxic effects toward HUVECs within the tested concentration range. Even at a dose of up to 200 $\mu g\ mL^{-1}$ and an incubation time of 24 h, HUVECs still exhibited a survival rate greater than 85%. By contrast, CCM@MIB induced a remarkable decline in the viability of 4T1 cells, as shown in Figure 5a. CCM@MIB has low cytotoxicity toward normal cells, while exhibiting apparent cytotoxicity to homologous tumor cells, which is of vital importance for utilization in cancer treatment. Meanwhile, CCM@MIB (as high as 600 $\mu g\ mL^{-1}$) also manifested a very low hemolysis effect, with a hemolysis rate of only 3.18 ± 0.43% (Figure S22), suggesting


https://doi.org/10.1021/acsami.5c01310
ACS Appl. Mater. Interfaces 2025, 17, 16681−16695

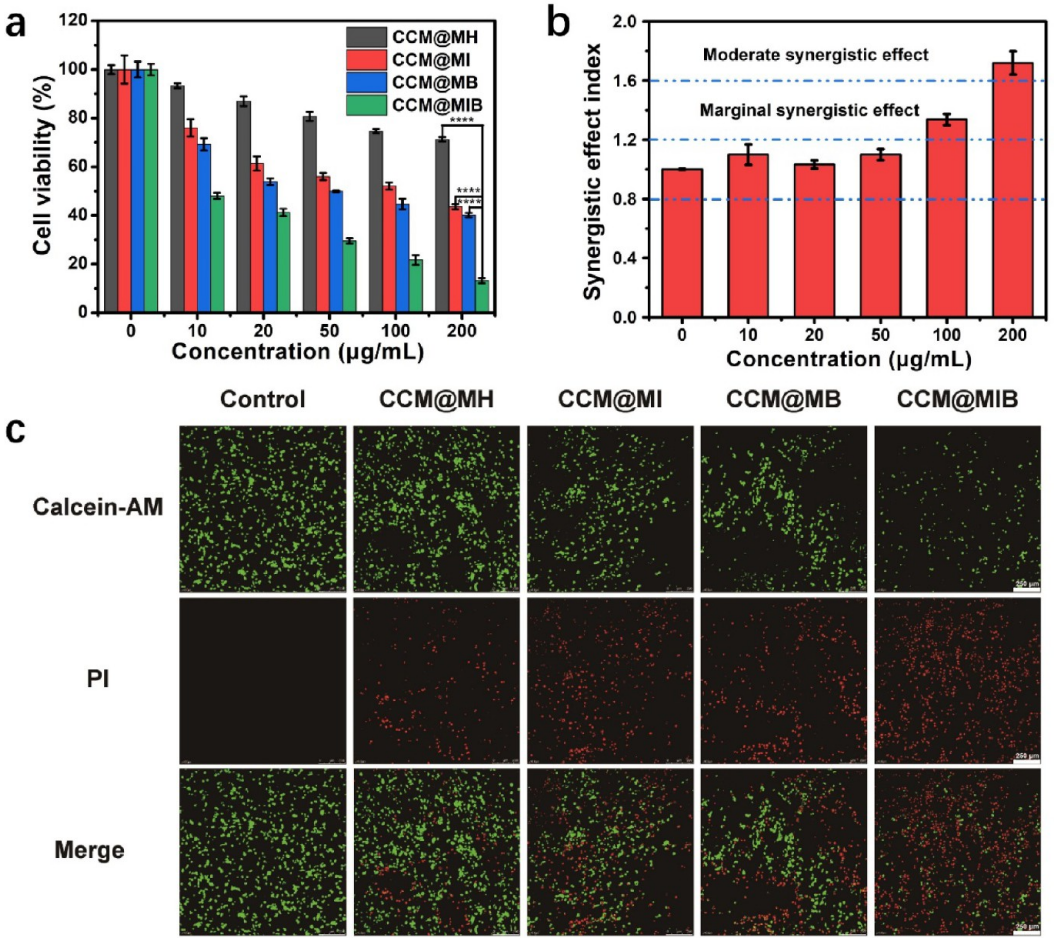


**Figure 5.** (a) Viability of tumor cells in various-treated groups. (b) Synergistic effect index of catalytic therapy and $SO_2$ GT on killing 4T1 cells using CCM@MIB. (c) Images of 4T1 cells (from confocal microscopy) by calcein-AM/PI costaining after varying therapies. Scale bar: 250 $\mu$m.

the safety of intravenous administration. The above results suggest that CCM@MIB exhibits satisfactory biocompatibility and biosafety, which are conducive to both *in vitro* and *in vivo* anticancer treatment research.

Subsequently, standard MTT was conducted to measure the viability of 4T1 cells after exposure to various treatments for evaluating *in vitro* therapeutic effect of CCM@MIB. Both CCM@MI and CCM@MB treatments induced similar toxic effects (Figure 5a) toward tumor cells (cell viability of 43.60 ± 1.05% and 40.16 ± 0.89% at 200 $\mu$g mL$^{-1}$, respectively), indicating that a single treatment of non-Fenton-type catalytic therapy or $SO_2$ GT could only kill part of the 4T1 cells. In contrast, the cell viability for the CCM@MIB group significantly decreased, dropping to as low as 13.20% (200 $\mu$g mL$^{-1}$), demonstrating that the cooperation of non-Fenton-generated •OH with $SO_2$ GT exhibits a remarkable killing efficacy on tumor cells. The calculated synergistic indexes[43] (Figure 5b) confirm that the combination therapy using CCM@MIB exhibited a good synergistic therapeutic performance, especially at 200 $\mu$g mL$^{-1}$.

Differently treated 4T1 cells were exposed to both calcein-AM and PI stainings to evaluate the therapeutic effects (Figure 5c). No apparent red FL has appeared in the control group. In contrast, some tumor cells treated with CCM@MI or CCM@MB were labeled with red FL, manifesting a limited ability of non-Fenton-type catalytic therapy or $SO_2$ GT alone to kill tumor cells. Notably, the most apparent red FL was detected in the CCM@MIB group, which indicates the optimum therapeutic effects, in accordance with the above results from MTT. Hence, an ingenious combination of non-Fenton-generated •OH and therapeutic gas $SO_2$ would significantly enhance the antitumor efficacy.

**3.7. *In Vitro* $SO_2$ Generation, ROS Production, and Antioxidation Enzyme System Detection.** To further explore the mechanism of *in vitro* therapy with CCM@MIB, the intracellular $SO_2$ level was first monitored with the probe DEACA after 4T1 cells were incubated with the nanomedicines. DEACA can enter the cells freely and reacts with $HSO_3^-$ (through a nucleophilic addition reaction) in cells to form the reaction product that can generate blue fluorescence.[30] Thus, DEACA was employed to monitor the intracellular $SO_2$ concentration. In comparison with the other three groups without visible FL, the tumor cells treated with CCM@MB or CCM@MIB that contains the donor BTS exhibited remarkable blue FL (Figures 6a and S23), indicating that CCM@MB and CCM@MIB could efficiently liberate $SO_2$ in the cells after internalization, and the acidic environment contributes to the intracellular generation of $SO_2$.

$SO_2$ is believed to be capable of scavenging GSH and upregulating ROS levels, thereby enhancing the efficacy of ROS-based treatment modalities.[14,44−47] Herein, we extensively investigated the inhibitory effect of $SO_2$ on important reductants and enzymes in the antioxidant system of tumors, including GSH, GPX4, and SOD.


https://doi.org/10.1021/acsami.5c01310
ACS Appl. Mater. Interfaces 2025, 17, 16681−16695

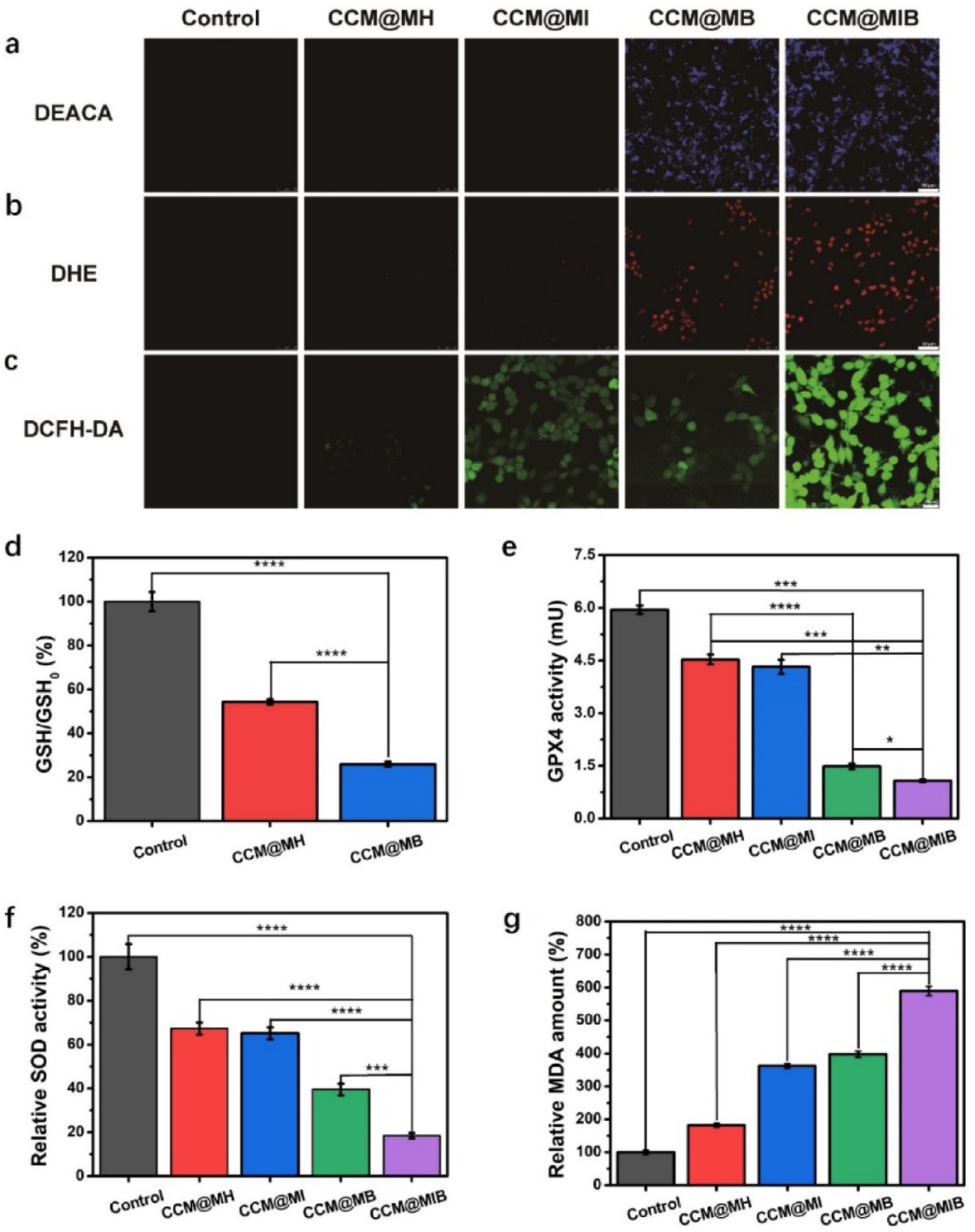


**Figure 6.** Detection images of intracellular $SO_2$ (Scale bar = 50 $\mu$m) (a), $\bullet O_2^-$ (Scale bar = 50 $\mu$m) (b), and ROS (Scale bar = 25 $\mu$m) (c) levels in 4T1 tumor cells after exposure to different treatments with respective probes, namely, DEACA, DHE, and DCFH-DA. Relative intracellular GSH levels (d), GPX4 activities (e), relative SOD activities (f), and MDA levels (g) of different treatment groups.

To investigate the *in vitro* GSH elimination capacity, the GSH levels in 4T1 cells exposed to various treatments were measured. The tumor cells incubated with CCM@MH showed ~45% GSH depletion due to the presence of $Mn^{3+}/Mn^{4+}$ in the hollow spheres, while CCM@MB increased the clearance rate of GSH to 75%, indicating that the released $SO_2$ also contributed significantly to GSH elimination (Figure 6d). The efficacious depletion of GSH by both MHs and the released $SO_2$ can protect the generated ROS from off-target consumption.[44,45] GSH clearance would directly lead to a decrease in GPX4 activity.[23,24] As indicated in Figure 6e, the intracellular GPX4 enzyme activities in the CCM@MB and CCM@MIB groups were significantly reduced to ~1.5 and 1.0 mU, respectively. The released $SO_2$ contributed more than 60% to the downregulation of GPX4 activity, which is due to


https://doi.org/10.1021/acsami.5c01310
ACS Appl. Mater. Interfaces 2025, 17, 16681−16695

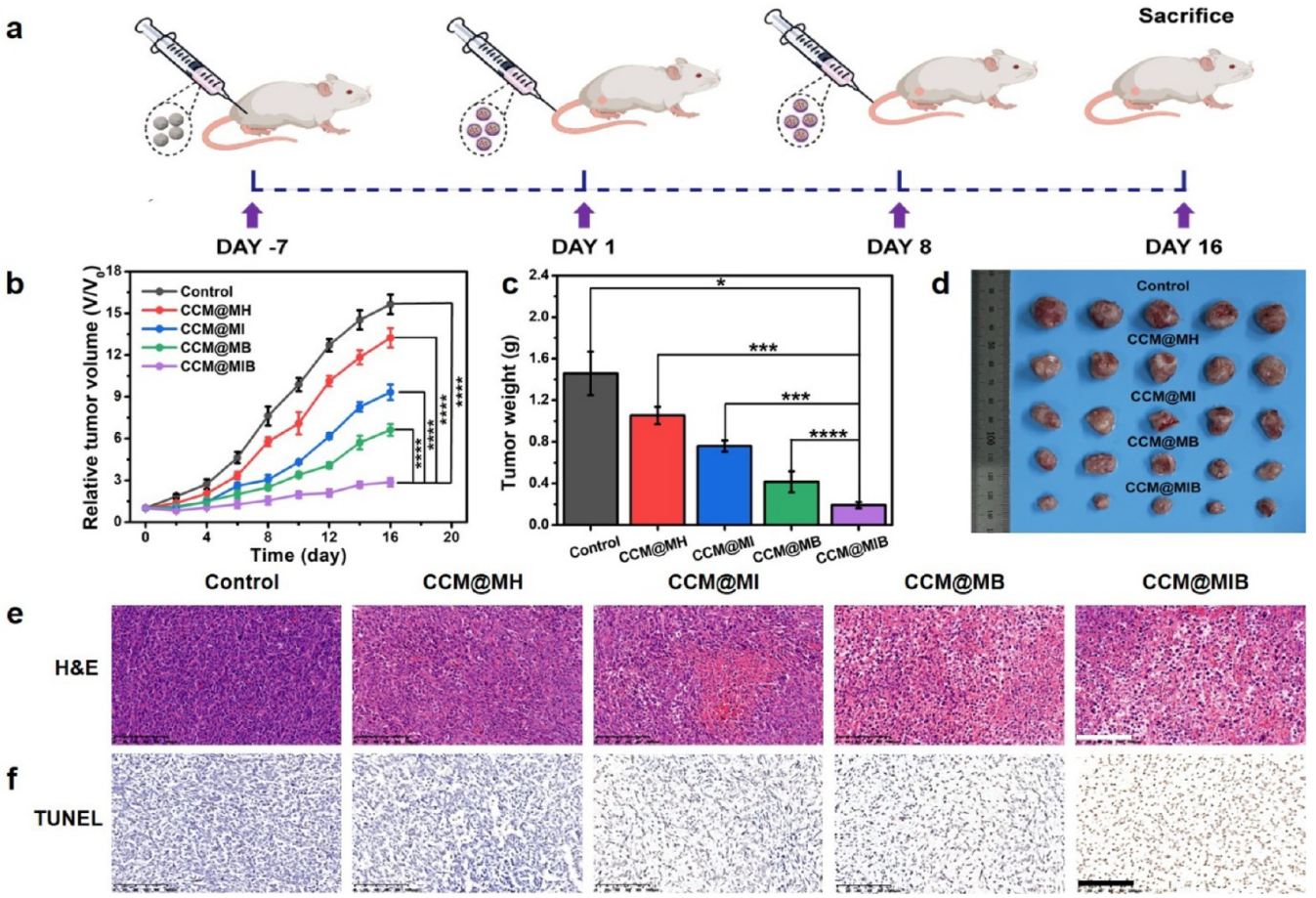


**Figure 7.** (a) Illustration that shows the construction of transplanted 4T1 tumor model and the corresponding treatment plan. (b) Curves of tumor volume within various groups. (c) Weights of the tumors dissected from different groups on the 16th day. (d) Photographs of tumors. Staining images (Scale bar = 100 $\mu$m) by H&E (e) and TUNEL (f) methods of tumor tissue sections.

the clearance of GSH by $SO_2$ and the possible direct interaction of $SO_2$ with GPX4.[19−21]

In addition to GPX4, $SO_2$ also affects the activity of SOD. As illustrated in Figure 6f, both the CCM@MB and CCM@MIB groups exhibited significantly weakened SOD activities. It is known that an apparent decrease in SOD activity would cause the enhancement of the intracellular $\bullet O_2^-$ level.[22] In view of this, the $\bullet O_2^-$ levels in 4T1 cells after being cultured with different nanocomposites were evaluated with DHE, an $\bullet O_2^-$-specific FL probe.[22] After it enters the cells, DHE is dehydrogenated by intracellular $\bullet O_2^-$ to form ethidium, which combines with DNA or RNA to emit red fluorescence. In comparison with the groups involving no $SO_2$ donors, the cells incubated with CCM@MB and CCM@MIB displayed significant red FL (Figures 6b and S24), confirming the raised $\bullet O_2^-$ level enabled by the liberated $SO_2$. In the self-oxidation of INH catalyzed by Mn ions, highly toxic •OH is produced from the intermediate product $\bullet O_2^-$. The upregulation of the $\bullet O_2^-$ level in tumor cells by $SO_2$ is beneficial to the production of •OH.[9]

In order to visually observe intracellular ROS production, differently treated tumor cells were stained by DCFH-DA. As illustrated in Figure 6c, the CCM@MH group exhibited very faint green FL, due to the intracellular ROS accumulation caused by GSH depletion. In comparison, bright green FL was detected in the CCM@MI group, implying abundant ROS generation due to the self-oxidation of INH catalyzed by $Mn^{2+}$ ions. A significant enhancement of green FL was also observed in the CCM@MB group, which means that more ROS was produced owing to the suppression of the antioxidant defense systems (including depletion of GSH and enzyme activity inhibition of SOD and GPX4) induced primarily by released $SO_2$. Importantly, the tumor cells treated with CCM@MIB presented the strongest green FL (Figure S25), revealing the disruption of intracellular redox balance and a ROS burst. The resulting strong oxidative stress can trigger LPO in cell membranes. The MDA level is commonly employed as an indicator to monitor the extent of LPO. As speculated, the CCM@MIB group exhibited an MDA level much higher than those of other treatment groups, suggesting that CCM@MIB caused the strongest LPO of tumor cell membranes (Figure 6g).

Considering that apoptosis is highly dependent on mitochondrial dysfunction, the mitochondrial integrity was also evaluated by the mitochondrial membrane potential assay kit with JC-1.[48] Compared to the control group with intact mitochondria, the CCM@MH group showed only weak green FL (Figure S26), indicating that the MH carriers caused no remarkable damage to mitochondrial function. Obvious green FL was found in both CCM@MI and CCM@MB groups, indicating that only a single treatment can cause mitochondrial damage to a certain extent. Especially, the CCM@MIB group exhibited the strongest green FL and weakest red FL, which implies a more remarkable decrease in the mitochondrial


https://doi.org/10.1021/acsami.5c01310
ACS Appl. Mater. Interfaces 2025, 17, 16681−16695

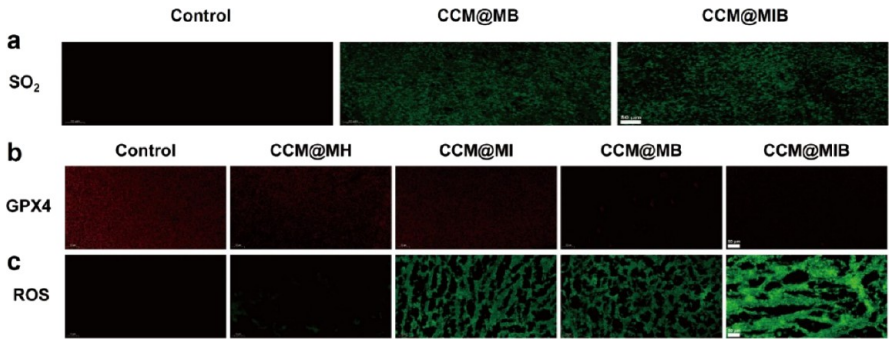


**Figure 8.** $SO_2$ release (a), GPX4 immunofluorescent staining (b), and ROS detection (c) of tumor tissues from varying treatment groups at 6 h after last injection of the materials. Scale bar: 50 $\mu$m.

membrane potential within tumor cells. Therefore, the high oxidative stress induced by the effective combination of non-Fenton-type catalytic therapy and $SO_2$ GT using CCM@MIB resulted in significant LPO and severe disruption of mitochondrial function, thus efficiently inhibiting the survival of tumor cells.

**3.8. *In Vivo* Antitumor Efficacy Assessment.** As *in vitro* treatment has achieved rather positive results mentioned above, *in vivo* antitumor effects of CCM@MIB were evaluated using the 4T1 tumor model (Figure 7a). Tumor-bearing mice were divided into five groups at random. Considering safety and pharmacodynamic efficacy, the nanomedicine dosage was determined to be 25 mg $kg^{-1}$. On days 1 and 8, CCM@MIB and other materials for comparison (25 mg $kg^{-1}$) were administered to the mice through intravenous injection. As indicated in Figure 7b, the growth trend for the tumor within the CCM@MH group was faintly lower than that of the PBS group, reflecting the slight tumor suppression effect of CCM@MH (a tumor suppression rate of 26.0% on the last day). The CCM@MI and CCM@MB groups displayed apparent antitumor efficacy (Figures 7b–d and S27) with final tumor suppression rates of 58.9% and 65.4%, respectively, due to the individual effect arising from the non-Fenton-generated ROS of CCM@MI and the released $SO_2$ of CCM@MB. Impressively, the CCM@MIB group demonstrated much better antitumor efficacy than other groups (tumor suppression rate high up to 84.9%), which is mainly contributed to the efficient synergy of $SO_2$ GT and non-Fenton-type catalytic therapy. The outstanding *in vivo* antitumor effect arising from CCM@MIB makes it promising in conquering deep tumors since it does not require external stimulation.

After the second injection of the nanomedicines for 6 h, TUNEL along with H&E stainings of tumor sections from the mice exposed to different treatments were performed to further evaluate the antitumor efficacy of combination therapy. Clearly, tumor tissues in the CCM@MIB group exhibited the highest apoptosis degree and the most serious damage compared with other groups, confirming satisfactory synergistic antitumor efficacy (Figure 7e,f).

To further reveal the antitumor mechanism of CCM@MIB, tumor sections were also prepared 6 h after the second injection for $SO_2$, GPX4, and ROS detection. The $SO_2$ release from CCM@MIB within the tumor tissues was under evaluation by DEACA. In comparison with the PBS group, apparent green FL was found in both the CCM@MB and CCM@MIB groups (Figures 8a and S28), indicating that a large amount of $SO_2$ was released in the tumor. In contrast, no obvious green FL signal was observed in the sections of the liver and spleen (Figure S29). It can be seen that both CCM@MB and CCM@MIB accumulated in tumors could respond to mildly acidic TME and efficiently generate $SO_2$, while almost no $SO_2$ is released in a normal physiological environment, which could reduce the toxicity arising from the nanomedicines on organs as well as normal tissues. Meanwhile, the lowest intracellular GPX4 enzyme activity was detected in the CCM@MIB group (Figures 8b and S30). It is known that the more GPX4 enzyme that is inactivated, the greater oxidative stress that occurs in tumor tissues.

Subsequently, tumor sections were stained with DCFH-DA to assess *in vivo* ROS generation in each group. The accumulation of ROS was observed in the CCM@MI and CCM@MB groups (Figures 8c and S31), which was caused by the self-oxidation of INH catalyzed by Mn ions and the efficient release of $SO_2$ from BTS, respectively. Expectedly, the brightest green FL that was remarkably stronger than the above two groups was detected in the CCM@MIB-treated mice (Figures 8c and S31), indicating the burst of ROS. Therefore, CCM@MIB accumulated in tumor tissues can significantly enhance oxidative stress in tumor cells by integrating non-Fenton •OH generation, acid-reactive $SO_2$ release, and antioxidant system destruction, thus achieving highly efficient antitumor treatment.

Finally, the biosafety of CCM@MIB in tumor treatment was evaluated. There was no significant body weight loss in all groups (Figure S32), which implies negligible side effects of CCM@MIB on the growth of mice. Moreover, the mice (the control and CCM@MIB groups) were euthanized after monitoring for 16 days to harvest blood, as well as the major organs for hematological and pathological analyses. Blood routine and biochemical indexes (kidney and liver) of the mice under treatment with CCM@MIB demonstrated no abnormal changes (Figure S33a–c). Meanwhile, negligible pathological abnormalities were exhibited in the H&E staining (major normal organs) (Figure S33d). Therefore, the CCM@MIB nanomedicine exhibits satisfactory biocompatibility and therapeutic biosafety.

## 4. CONCLUSIONS

In summary, the elaborately constructed CCM@MIB nanomedicine has demonstrated outstanding merits for tumor therapy. The homologous CCM camouflage significantly enhances the targeted accumulation of the nanomedicine toward tumor sites. In response to reducing and acidic TME, the nanocarrier MHs liberate Mn ions efficiently and the degradation process leads to the consumption of GSH and the downregulation of GPX4 to a certain extent. The released Mn


https://doi.org/10.1021/acsami.5c01310
ACS Appl. Mater. Interfaces 2025, 17, 16681–16695

ions subsequently catalyze the self-oxidation of INH to generate highly toxic •OH. Notably, the $SO_2$ released by the loaded donor in response to acidic TME can efficiently disrupt the tumor antioxidant system, including diminution of intracellular GSH levels and inhibition of GPX4 and SOD enzyme activities. Meanwhile, the CAT activity of MHs and the increased intracellular $•O_2^-$ level induced by $SO_2$ further contribute to the production of •OH. Consequently, the synergistic effect of non-Fenton-type catalytic therapy and $SO_2$ GT leads to a particularly high level of oxidative stress within tumor cells, thus efficaciously suppressing tumor growth. Additionally, the advantage of CCM@MIB in releasing Mn ions specifically at tumor sites makes it an activated MRI contrast agent for guiding and monitoring antitumor treatment. The developed CCM@MIB nanomedicine for synergistic non-Fenton-type catalytic-$SO_2$ GT provides a new idea for designing efficient treatment strategies to conquer deep tumors.

## ■ ASSOCIATED CONTENT

### Supporting Information

The Supporting Information is available free of charge at https://pubs.acs.org/doi/10.1021/acsami.5c01310.

SEM image, TEM image, and particle size distribution of $SiO_2$ nanoparticles; SEM image of MHs; particle size and shell thickness distribution of MHs; energy-dispersive spectroscopy spectrum of MHs; $N_2$ adsorption−desorption isotherm of MHs and pore size distribution of MHs; XRD pattern of MHs; XPS survey spectrum of MHs; $^1$H NMR and $^{13}$C NMR spectra of BTS; UV−vis spectra of BTS; standard curve of BTS, UV−vis spectra of INH, standard curve of INH, and UV−vis spectra of residual BTS and INH; Zeta potential and hydrodynamic size distribution of CCM@MIB and photograph of CCM@MIB dispersions; release curves of Mn ions from MIB; mechanism for detecting GSH by DTNB, GSH depletion ability of MHs, and relative GSH depletion capacity of MHs and MB; the reaction of TMB with ROS, absorption spectra for evaluating the oxidation of TMB in MIB solutions; changes in the absorption spectra of TMB; dissolved $O_2$ levels; the reaction of DEACA with $NaHSO_3$, normalized FL spectra (BTS and DEACA cocultured), $SO_2$ release from BTS, and normalized FL spectra (MIB and DEACA coincubated); $1/T_1$ and $1/T_2$ versus Mn concentration curves of MIB, $T_1$-weighted MRI images for MIB; *in vivo* biodistribution of Mn; Mn content of tumor sites; viability of HUVECs cultured with CCM@MIB; hemolysis evaluation data of CCM@MIB; mean fluorescence intensity (MFI) of DEACA, DHE, and 2,7-dichlorofluorescein in various groups; mitochondrial membrane potential in 4T1 cells; photographs of tumor-bearing mice; MFI of DEACA in tumor sections; $SO_2$ release in liver and spleen; MFI of GPX4 detection in tumor sections; MFI of 2,7-dichlorofluorescein in tumor sections; body weight change; and biocompatibility evaluation of various treatments (PDF)

## ■ AUTHOR INFORMATION


### Corresponding Author

**Huixia Wu** − *The Education Ministry Key Lab of Resource Chemistry, Joint International Research Laboratory of Resource Chemistry, Ministry of Education, Shanghai Key Laboratory of Rare Earth Functional Materials, Shanghai Municipal Education Committee Key Laboratory of Molecular Imaging Probes and Sensors, and Shanghai Frontiers Science Center of Biomimetic Catalysis, College of Chemistry and Materials Science, Shanghai Normal University, Shanghai 200234, China;* orcid.org/0000-0002-3945-542X; Email: wuhuixia@shnu.edu.cn

### Authors

**Shasha Zhao** − *The Education Ministry Key Lab of Resource Chemistry, Joint International Research Laboratory of Resource Chemistry, Ministry of Education, Shanghai Key Laboratory of Rare Earth Functional Materials, Shanghai Municipal Education Committee Key Laboratory of Molecular Imaging Probes and Sensors, and Shanghai Frontiers Science Center of Biomimetic Catalysis, College of Chemistry and Materials Science, Shanghai Normal University, Shanghai 200234, China*

**Zhonghuan Qu** − *The Education Ministry Key Lab of Resource Chemistry, Joint International Research Laboratory of Resource Chemistry, Ministry of Education, Shanghai Key Laboratory of Rare Earth Functional Materials, Shanghai Municipal Education Committee Key Laboratory of Molecular Imaging Probes and Sensors, and Shanghai Frontiers Science Center of Biomimetic Catalysis, College of Chemistry and Materials Science, Shanghai Normal University, Shanghai 200234, China*

**Likai Wang** − *The Education Ministry Key Lab of Resource Chemistry, Joint International Research Laboratory of Resource Chemistry, Ministry of Education, Shanghai Key Laboratory of Rare Earth Functional Materials, Shanghai Municipal Education Committee Key Laboratory of Molecular Imaging Probes and Sensors, and Shanghai Frontiers Science Center of Biomimetic Catalysis, College of Chemistry and Materials Science, Shanghai Normal University, Shanghai 200234, China*

**Peng Gu** − *The Education Ministry Key Lab of Resource Chemistry, Joint International Research Laboratory of Resource Chemistry, Ministry of Education, Shanghai Key Laboratory of Rare Earth Functional Materials, Shanghai Municipal Education Committee Key Laboratory of Molecular Imaging Probes and Sensors, and Shanghai Frontiers Science Center of Biomimetic Catalysis, College of Chemistry and Materials Science, Shanghai Normal University, Shanghai 200234, China*

**Juan Mou** − *The Education Ministry Key Lab of Resource Chemistry, Joint International Research Laboratory of Resource Chemistry, Ministry of Education, Shanghai Key Laboratory of Rare Earth Functional Materials, Shanghai Municipal Education Committee Key Laboratory of Molecular Imaging Probes and Sensors, and Shanghai Frontiers Science Center of Biomimetic Catalysis, College of Chemistry and Materials Science, Shanghai Normal University, Shanghai 200234, China;* orcid.org/0000-0002-1822-5318

**Shiping Yang** − *The Education Ministry Key Lab of Resource Chemistry, Joint International Research Laboratory of Resource Chemistry, Ministry of Education, Shanghai Key Laboratory of Rare Earth Functional Materials, Shanghai Municipal Education Committee Key Laboratory of Molecular Imaging Probes and Sensors, and Shanghai Frontiers Science Center of Biomimetic Catalysis, College of*

*Chemistry and Materials Science, Shanghai Normal University, Shanghai 200234, China;* orcid.org/0000-0001-7527-4581

Complete contact information is available at: https://pubs.acs.org/10.1021/acsami.5c01310

### Author Contributions

#S.Z., Z.Q., and L.W. contributed equally to this work and should be regarded as the first coauthors. The manuscript was written through contributions of all authors. All authors have given approval to the final version of the manuscript.

### Notes

The authors declare no competing financial interest.

## ■ ACKNOWLEDGMENTS

This work was supported by the Shanghai Municipal Natural Science Foundation (20ZR1441400), the National Natural Science Foundation of China (91959105), the General Scientific Research Project of Shanghai Normal University (309-AW0203-23-005316), the "111" Innovation and Talent Recruitment Base on Photochemical and Energy Materials (D18020), and the Shanghai Engineering Research Center of Green Energy Chemical Engineering (18DZ2254200).

## ■ REFERENCES

(1) Tang, Z. M.; Liu, Y. Y.; He, M. Y.; Bu, W. B. Chemodynamic Therapy: Tumour Microenvironment-Mediated Fenton and Fenton-Like Reactions. *Angew. Chem. Int. Ed.* **2019**, *58*, 946−956.

(2) Chen, M. Y.; Dong, C. Y.; Shi, S. An Overview of Recent Advancements on Manganese-Based Nanostructures and Their Application for ROS-Mediated Tumor Therapy. *ACS Mater. Lett.* **2022**, *4*, 2415−2433.

(3) Li, S.-L.; Chu, X.; Dong, H. L.; Hou, H. Y.; Liu, Y. Recent Advances in Augmenting Fenton Chemistry of Nanoplatforms for Enhanced Chemodynamic Therapy. *Coordin. Chem. Rev.* **2023**, *479*, 215004.

(4) Shen, Z. Y.; Liu, T.; Li, Y.; Lau, J.; Yang, Z.; Fan, W. P.; Zhou, Z. J.; Shi, C. R.; Ke, C. M.; Bregadze, V. I.; Mandal, S. K.; Liu, Y. J.; Li, Z. H.; Xue, T.; Zhu, G. Z.; Munasinghe, J.; Niu, G.; Wu, A. G.; Chen, X. Y. Fenton-Reaction-Acceleratable Magnetic Nanoparticles for Ferroptosis Therapy of Orthotopic Brain Tumors. *ACS Nano* **2018**, *12*, 11355−11365.

(5) Zhang, Y. J.; Chen, P. H.; Li, B. H.; Guo, H. S.; Zhu, J. F.; Dang, Z. C.; Lei, S.; Huang, P.; Lin, J. Comprehensively Optimizing Fenton Reaction Factors for Antitumor Chemodynamic Therapy by Charge-Reversal Theranostics. *ACS Nano* **2023**, *17*, 16743−16756.

(6) Zhu, Y.; Gong, P.; Wang, J.; Cheng, J. J.; Wang, W. Y.; Cai, H. L.; Ao, R. J.; Huang, H. W.; Yu, M. L.; Lin, L. S.; et al. Amplification of Lipid Peroxidation by Regulating Cell Membrane Unsaturation to Enhance Chemodynamic Therapy. *Angew. Chem. Int. Ed.* **2023**, *62*, No. e202218407.

(7) Lu, J. Y.; Yang, Y. Q.; Xu, Q. Q.; Lin, Y. Z.; Feng, S. P.; Mao, Y. L.; Wang, D.; Wang, S. L.; Zhao, Q. F. Recent Advances in Multi-Configurable Nanomaterials for Improved Chemodynamic Therapy. *Coordin. Chem. Rev.* **2023**, *474*, 214861.

(8) Zhang, J.; Lovell, J. F.; Shi, J. F.; Zhang, Y. M. Nanomaterials for Co-immobilization of Multiple Enzymes. *BMEMat* **2024**, No. e12080.

(9) Ito, K.; Yamamoto, K.; Kawanishi, S. Manganese-Mediated Oxidative Damage of Cellular and Isolated DNA by Isoniazid and Related Hydrazines: Non-Fenton-Type Hydroxyl Radical Formation. *Biochemistry* **1992**, *31*, 11606.

(10) Cheng, Y. R.; Yang, F.; Zhang, K.; Zhang, Y. Y.; Cao, Y.; Liu, C. H.; Lu, H. T.; Dong, H. F.; Zhang, X. J. Non-Fenton-Type Hydroxyl Radical Generation and Photothermal Effect by Mitochondria-Targeted WSSe/$MnO_2$ Nanocomposite Loaded with Isoniazid for Synergistic Anticancer Treatment. *Adv. Funct. Mater.* **2019**, *29*, 1903850.

(11) Cui, M. J.; Xu, B.; Wang, L. H. Recent Advances in Multi-Metallic-Based Nanozymes for Enhanced Catalytic Cancer Therapy. *BMEMat* **2024**, *2* (1), No. e12043.

(12) Khan, M. A.; Tania, M.; Zhang, D.-Z.; Chen, H. C. Antioxidant Enzymes and Cancer. *Chin. J. Cancer Res.* **2010**, *22*, 87−92.

(13) Bansal, A.; Simon, M. C. Glutathione Metabolism in Cancer Progression and Treatment Resistance. *J. Cell Biol.* **2018**, *217*, 2291−2298.

(14) Zhang, T.; Pan, Y.; Suo, M.; Lyu, M.; Lam, J. W. Y.; Jin, Z.; Ning, S.; Tang, B. Photothermal-Triggered Sulfur Oxide Gas Therapy Augments Type I Photodynamic Therapy for Potentiating Cancer Stem Cell Ablation and Inhibiting Radioresistant Tumor Recurrence. *Adv. Sci.* **2023**, *10*, 2304042.

(15) Huang, Y. Q.; Tang, C. S.; Du, J. B.; Jin, H. F.; Bian, J.-S. Endogenous Sulfur Dioxide: A New Member of Gasotransmitter Family in the Cardiovascular System. *Oxid. Med. Cell. Longevity* **2016**, *2016*, 8961951.

(16) Ding, H.; Wei, J.; Fang, L.; Feng, L.; Gai, S.; He, F.; Wu, L. Z.; Rehman, Z.; Yang, P. P. A Multichannel Metabolic Pathway Interference Strategy for Complete Energy Depletion-Mediated Cancer Therapy. *Adv. Funct. Mater.* **2024**, *34*, 2312429.

(17) Wang, Y. S.; Yang, T.; He, Q. J. Strategies for Engineering Advanced Nanomedicines for Gas therapy of Cancer. *Natl. Sci. Rev.* **2020**, *7*, 1485−1512.

(18) Mannervik, B.; Persson, G.; Eriksson, S. Enzymatic Catalysis of the Reversible Sulfitolysis of Glutathione Disulfide and the Biological Reduction of Thiosulfate Esters. *Arch. Biochem. Biophys.* **1974**, *163*, 283−289.

(19) Langley-Evans, S. C.; Phillips, G. J.; Jackson, A. A. Sulphur Dioxide: A Potent Glutathione Depleting Agent. *Comp. Biochem. Physiol. C Pharmacol. Toxicol. Endocrinol.* **1996**, *114*, 89−98.

(20) Cheng, X. T.; Xu, H. D.; Ran, H. H.; Liang, G. L.; Wu, F. G. Glutathione-Depleting Nanomedicines for Synergistic Cancer Therapy. *ACS Nano* **2021**, *15*, 8039−8068.

(21) Meng, Z. Q. Oxidative Damage of Sulfur Dioxide on Various Organs of Mice: Sulfur Dioxide is A Systemic Oxidative Damage Agent. *Inhal. Toxicol.* **2003**, *15*, 181−195.

(22) Gu, R.; Wang, L.; Huang, X. Y.; Zhang, J. Y.; Ou, C. J.; Si, W. L.; Yu, J. G.; Wang, W. J.; Dong, X. C. PH/Glutathione-Responsive Release of $SO_2$ Induced Superoxide Radical Accumulation for Gas Therapy of Cancer. *Chem. Commun.* **2020**, *56*, 14865−14868.

(23) Xia, M. J.; Guo, Z. H.; Liu, X. M.; Wang, Y.; Xiao, C. S. A Glutathione-Eesponsive Sulfur Dioxide Polymer Prodrug Selectively Induces Ferroptosis in Gastric Cancer Therapy. *Biomater. Sci.* **2022**, *10*, 4184.

(24) Tang, H. X.; Li, C. Q.; Zhang, Y.; Zheng, H. Y.; Cheng, Y.; Zhu, J. J.; Chen, X. J.; Zhu, Z. H.; Piao, J.-G.; Li, F. Z. Targeted Manganese Doped Silica Nano GSH-Cleaner for Treatment of Liver Cancer by Destroying the Intracellular Redox Homeostasis. *Theranostics* **2020**, *10*, 9865−9887.

(25) Cao, S.; Dong, S.; Feng, L.; Wei, N.; Xie, Y.; Dong, Y.; Zhu, Y.; Zhao, R.; He, F.; Yang, P. Engineering Strain-Defects to Enhance Enzymatic Therapy and Induce Ferroptosis. *Adv. Mater.* **2024**, *36*, 2408502.

(26) Giles, G. I.; Jacob, C. Reactive Sulfur Species: An Emerging Concept in Oxidative Stress. *Biol. Chem.* **2002**, *383*, 375−388.

(27) Li, S. H.; Liu, R.; Jiang, X. X.; Qiu, Y.; Song, X. R.; Huang, G. M.; Fu, N. Y.; Lin, L. S.; Song, J. B.; Chen, X. Y.; et al. Near-Infrared Light-Triggered Sulfur Dioxide Gas Therapy of Cancer. *ACS Nano* **2019**, *13*, 2103−2113.

(28) Shen, W.; Liu, W. G.; Yang, H. L.; Zhang, P.; Xiao, C. S.; Chen, X. S. A Glutathione-Responsive Sulfur Dioxide Polymer Prodrug as A Nanocarrier for Combating Drug-Resistance in Cancer Chemotherapy. *Biomaterials* **2018**, *178*, 706−719.

(29) Yao, X.; Ma, S.; Peng, S.; Zhou, G.; Xie, R.; Jiang, Q.; Guo, S.; He, Q.; Yang, W. Zwitterionic Polymer Coating of Sulfur Dioxide-

Releasing Nanosystem Augments Tumor Accumulation and Treatment Efficacy. *Adv. Healthcare Mater.* **2020**, *9*, 1901582.
(30) Lu, Q. L.; Lu, T.; Xu, M.; Yang, L. F.; Song, Y. L.; Li, N. $SO_2$ Prodrug Doped Nanorattles with Extra-High Drug Payload for "Collusion inside and outside" Photothermal/pH Triggered-Gas Therapy. *Biomaterials* **2020**, *257*, 120236.
(31) Gong, X.; Li, J.; Tan, T.; Wang, W. Z.; Wang, H.; Wang, Y. Q.; Xu, X. X.; Zhang, Z. W.; Li, Y. P. Emerging Approaches of Cell-Based Nanosystems to Target Cancer Metastasis. *Adv. Funct. Mater.* **2019**, *29*, 1903441.
(32) Pan, W. L.; Tan, Y.; Meng, W.; Huang, N. H.; Zhao, Y. B.; Yu, Z. Q.; Huang, Z.; Zhang, W. H.; Sun, B.; Chen, J. X. Microenvironment-driven sequential ferroptosis, photodynamic therapy, and chemotherapy for targeted breast cancer therapy by a cancer-cell-membrane-coated nanoscale metal-organic framework. *Biomaterials* **2022**, *283*, 121449.
(33) Yu, L. D.; Chen, Y.; Wu, M. Y.; Cai, X. J.; Yao, H. L.; Zhang, L. L.; Chen, H. R.; Shi, J. L. Manganese Extraction" Strategy Enables Tumor-Sensitive Biodegradability and Theranostics of Nanoparticles. *J. Am. Chem. Soc.* **2016**, *138*, 9881−9894.
(34) Tian, H.; Zeng, L.; Huang, Y.; Ma, Z.; Meng, G.; Peng, L.; Chen, C.; Cui, X.; Shi, J. In Situ Electrochemical Mn(III)/Mn(IV) Generation of Mn(II)O Electrocatalysts for High-Performance Oxygen Reduction. *Nano-Micro Lett.* **2020**, *12*, 161.
(35) Shih, Y. J.; Chen, Z. S.; Chen, C.-L.; Huang, Y. H.; Huang, C. P. Enhancing Arsenic (III) Removal by Integrated Electrocatalytic Oxidation and Electrosorption Reactions on Nano-Textured Bimetal Composite of Iron Oxyhydroxide and Manganese Dioxide Polymorphs ($\alpha$-, $\gamma$-, $\beta$-, and $\varepsilon$-$Mn_xFe_{1-x}O$). *Appl. Catal., B* **2022**, *317*, 121757.
(36) Zálešák, F.; Kováč, O.; Lachetová, E.; Šťastná, N.; Pospíšil, J. Unified Approach to Benzo[d]thiazol-2-yl-sulfonamides. *J. Org. Chem.* **2021**, *86*, 11291−11309.
(37) Zhao, C. L.; Liu, X.; Zhang, X.; Yan, H.; Qian, Z. L.; Li, X. H.; Ma, Z. Y.; Han, Q. R.; Pei, C. H. A Facile One-Step Method for Preparation of $Fe_3O_4$/CS/INH Nanoparticles as A Targeted Drug Delivery for Tuberculosis. *Mater. Sci. Eng., C* **2017**, *77*, 1182−1188.
(38) Tian, B. S.; Tian, R. X.; Liu, S. H.; Wang, Y.; Gai, S. L.; Xie, Y.; Yang, D.; He, F.; Yang, P. P.; Lin, J. Doping Engineering to Modulate Lattice and Electronic Structure for Enhanced Piezocatalytic Therapy and Ferroptosis. *Adv. Mater.* **2023**, *35*, 2304262.
(39) Zhu, P.; Pu, Y. Y.; Wang, M.; Wu, W. C.; Qin, H. L.; Shi, J. L. MnOOH-Catalyzed Autoxidation of Glutathione for Reactive Oxygen Species Production and Nanocatalytic Tumor Innate Immunotherapy. *J. Am. Chem. Soc.* **2023**, *145*, 5803−5815.
(40) Zhang, F.; Cheng, K.; Huang, Z. Y.; Hou, X. L.; Zhang, X. S.; Zhong, Z. T.; Hu, Y. G.; Lei, X. L.; Li, Y.; Zhang, P. J.; et al. Tumor Microenvironment-Responsive Nanocarrier Based on $VO_x$ Nanozyme Amplify Oxidative Stress for Tumor Therapy. *Adv. Funct. Mater.* **2023**, *33*, 2212740.
(41) Day, J. J.; Yang, Z. H.; Chen, W.; Pacheco, A.; Xian, M. Benzothiazole Sulfinate: A Water-Soluble and Slow-Releasing Sulfur Dioxide Donor. *ACS Chem. Biol.* **2016**, *11*, 1647−1651.
(42) Xu, M.; Lu, Q. L.; Song, Y. L.; Yang, L. F.; Li, J. N.; Li, N. Enhanced Bax Upregulating in Mitochondria for Deep Tumor Therapy Based on $SO_2$ Prodrug Loaded Au−Ag Hollow Nanotriangles. *Biomaterials* **2020**, *250*, 120076.
(43) Liu, J.; Wu, Y.; Fu, C.; Li, B.; Li, L.; Zhang, R.; Xu, T.; Xu, Z. Charge Reversion Simultaneously Enhances Tumor Accumulation and Cell Uptake of Layered Double Hydroxide Nanohybrids for Effective Imaging and Therapy. *Small* **2020**, *16*, 2002115.
(44) Chen, T.; Luo, X.; Zhu, L. W.; Xiang, J. F.; Fang, C. F.; Zhu, D. M.; Li, G. X.; Duo, Y. H. Biomimetic Single-Atom Nanozyme System for Efficient Inhibition of Gastric Cancer Ascites via $SO_2$ Gas-Enhanced Nanocatalytic Cancer Therapy. *Chem. Eng. J.* **2023**, *467*, 143386.
(45) Liang, J.; Cheng, G.; Qiu, L.; Xue, L.; Xu, H.; Qiao, X.; Guo, N.; Xiang, H.; Chen, Y.; Ding, H. Activatable Sulfur Dioxide Nanosonosensitizer Enables Precisely Controllable Sono-Gaseous Checkpoint Trimodal Therapy for Orthotopic Hepatocellular Carcinoma. *Adv. Sci.* **2025**, *12*, 2409442.
(46) Zhang, Y.; Zhang, H. Y.; Wang, Y. F.; Ji, Y. Y.; Wang, F.; He, P. A Novel Cu(II) Loaded Polypeptide $SO_2$ Prodrug Nanoformulation Combining Chemodynamic and Gas Anticancer Therapies. *Macromol. Biosci.* **2024**, *24*, 2300429.
(47) Zhang, Y.; Shen, W.; Zhang, P.; Chen, L.; Xiao, C. S. GSH-Triggered Release of Sulfur Dioxide Gas to Regulate Redox Balance for Enhanced Photodynamic Therapy. *Chem. Commun.* **2020**, *56*, 5645−5648.
(48) Du, F.; Liu, L.; Wu, Z.; Zhao, Z.; Geng, W.; Zhu, B.; Ma, T.; Xiang, X.; Ma, L.; Cheng, C.; Qiu, L. Pd-Single-Atom Coordinated Biocatalysts for Chem-/Sono-/Photo-Trimodal Tumor Therapies. *Adv. Mater.* **2021**, *33*, 2101095.


https://doi.org/10.1021/acsami.5c01310
*ACS Appl. Mater. Interfaces* 2025, 17, 16681−16695